Biogeosciences

Performance of temperature and productivity proxies based on long-chain alkane-1, mid-chain diols at test: a 5-year sediment trap record from the Mauritanian upwelling

Gerard J. M. Versteegh[1,2,3], **Karin A. F. Zonneveld**[3,4], **Jens Hefter**[1,3], **Oscar E. Romero**[1,3], **Gerhard Fischer**[4], and **Gesine Mollenhauer**[1,3]

[1]Alfred Wegener Institute for Polar and Marine Research, Am Handelshafen 12, 27570 Bremerhaven, Germany
[2]Department of Physics and Earth Sciences, Jacobs University, Bremen, 28759 Bremen, Germany
[3]MARUM – Zentrum für Marine Umweltwissenschaften, Universität Bremen, 28359 Bremen, Germany
[4]Fachbereich Geowissenschaften, Universität Bremen, 28359 Bremen, Germany

Correspondence: Gerard J. M. Versteegh (versteeg@uni-bremen.de, gerard.versteegh@awi.de)

Abstract. Proxies based on long-chain alkane-1, mid-chain diols (diol for short) are obtaining increasing interest to reconstruct past upper ocean temperature and productivity. Here we evaluate performance of the sea surface temperature proxies (long-chain diol index (LDI), diol saturation index (DSI), and diol chain length index (DCI)), productivity and upwelling intensity proxies (two diol indices DI_R and DI_W and the combined diol index (CDI)), and the nutrient diol index (NDI) as a proxy for phosphate and nitrate levels. This evaluation is based on comparison of the diols in sediment trap samples from the upwelling region off NW Africa collected at 1.28 km water depth with daily satellite-derived sea surface temperatures (SSTs), subsurface temperatures, productivity, the plankton composition from the trap location, monthly phosphate and nitrate concentrations, wind speed, and wind direction from the nearby Nouadhibou airport. The diol-based SST reconstructions are also compared the long-chain-alkenone-based SST reconstructions.

The alkenone SSTs correlate best with satellite SST ($r^2 = 0.60$). Amplitude and absolute values agree very well as do the flux-corrected time series averages. For the diol proxies the situation is more complicated.

Diol proxies including 1,14 diols lag trade wind speed by 30 d. Since wind is nearly always from the NNE to NNW and induces the upwelling, we relate the variability in these proxies to upwelling-induced processes. Correlation with the abundance of upwelling species and wind speed is best for the NDI and the 1,14 diol-based DCI and DSI. The DI_R, DI_W, and CDI perform comparatively poorly. A negative correlation between DSI and wind speed may suggest that the DSI reflects wind-speed-forced upwelling-related reductions in temperature rather than irradiation-induced temperatures. The nutrient proxy NDI shows no significant correlation to monthly phosphate and nitrate concentrations in the upper waters and a negative correlation with both wind-induced upwelling ($r^2 = 0.28$ and lagging 32 d) and the abundance of upwelling species ($r^2 = 0.38$). It is suggested that this proxy reflects upwelling intensity rather than upper ocean nutrient concentrations.

At the trap site, satellite SST lags wind-speed-forced upwelling by about 4 months. The 1,13 and 1,15 diol-based LDI-derived SSTs lag satellite SSTs by 41 d but correlate poorly ($r^2 = 0.17$). Absolute as well as flux-corrected LDI SSTs are on average 3 °C too high and rather reflect values prevailing during the more oligotrophic summer period. We attribute outliers to low LDI SST to 1,13 diols added during short upwelling-related events. The use of the LDI in regions with higher productivity is therefore not recommended.

It appears thus that at the trap site the 1,14 diols primarily reflect conditions relating to upwelling whereas the $1,15C_{30}$ and to a lesser extent the 1,13 diols seem to reflect the conditions of the more oligotrophic ocean.

1 Introduction

Upper ocean temperature and productivity reconstructions are important for assessing past climate and environment. For organisms, optimal functioning of their membranes and transport in the cell are crucial, and since temperature has a large influence on the solubility and viscosity of lipids, organisms adapt their lipid composition to temperature. Common responses to a decrease in temperature are (1) reduction of the average chain length of the lipid molecules and (2) an increase in the number of double bonds or (3) the degree of cyclization (e.g. Suutari et al., 1994; Elling et al., 2015; Sollich et al., 2017). We can use this response of organisms to adapt their metabolism and metabolite composition to prevailing ocean conditions to reconstruct past ocean temperature and productivity through searching for relevant metabolites in the fossil record and taking them as environmental proxies. This is not an unequivocal enterprise since the metabolite composition of organisms is often influenced by a combination of environmental variables, and, therefore, proxies based on these metabolites bear the risk of reflecting this. Furthermore, the same metabolites may be produced by different organisms, each having its own complex response to environment. To obtain robust and reliable temperature, nutrient, and productivity reconstructions from fossil metabolites, it is essential to test the performance of these proxies in present-day conditions. In this study, we do so by investigating the long-chain mid-chain diol composition in sediment trap samples in relation to environment during a multiyear trap deployment. We performed this study in the upwelling area off Cape Blanc, one of the most productive regions in the world (Chavez and Messié, 2009). From this region detailed (daily to monthly) records of water temperature, productivity, nutrient concentrations, and upwelling dynamics in the upper ocean as well as atmospheric parameters like wind direction and wind intensity are available.

Our study focuses on several diol-based proxies that have been proposed for temperature, productivity, and/or upper ocean nutrient concentrations. For temperature these are (1) the long-chain diol index (LDI) (Rampen et al., 2012), (2) the diol saturation index (DSI) (Rampen et al., 2014a), and (3) the diol chain length index (DCI) (Rampen et al., 2009, 2014a). The combined diol index (CDI) (Rampen et al., 2014a) and two diol indices (DI), the DI_R (Rampen et al., 2008) and DI_W (Willmott et al., 2010), have been suggested as proxies for upper ocean upwelling and productivity. The nutrient diol index (NDI) has been proposed for reconstructing sea surface nitrate and phosphate concentrations (Gal et al., 2018).

Other diol-based proxies have been defined but these either strongly correlate with the proxies mentioned above or are not relevant in the Mauritanian setting such as a diol proxy for terrestrial and fresh water input (Versteegh et al., 1997; Lattaud et al., 2017a, b). We also evaluate the diol temperature proxies in relation to the lipid-based temperature
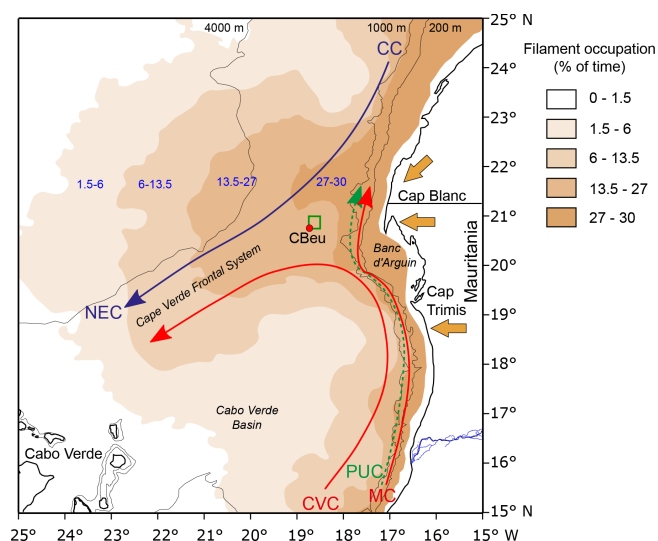

Figure 1. The Mauritanian upwelling system. CC, Canary Current; NEC, North Equatorial Current; CVC, Cap Verde Current; MC, Mauritanian Current; PUC, Poleward Under Current. The red circle in the lower left corner of the small green square marks the location of mooring CBeu. The green square represents the upstream $0.25° \times 0.25°$ area from which sea surface data have been obtained.

proxy: the long-chain-alkenone-based $U_{37}^{K'}$ (Prahl and Wakeham, 1987; Brassell et al., 1986).

Regional oceanography

The Mauritania upwelling system is part of the Canary Current (CC) Eastern Boundary Upwelling Ecosystem (CC-EBUE). The coastal upwelling off Mauritania is driven by the NNW-to-NNE trade winds and occurs where the southward CC flowing along the coast meets the northward Cap Verde Current (CVC) and Poleward Undercurrent (PUC). These currents are deflected offshore, resulting in the SW-directed Cape Verde Frontal Zone (CVFZ) (Fig. 1). The result of this deflection and the offshore water export is visible as the giant Mauritanian chlorophyll filament (Fig. 1 after Romero et al., 2020 and Lovecchio et al., 2018). As a result of the coastal, shelf, and slope topography and the ocean currents and trade winds from the north, the coastal region off Mauritania is characterized by almost permanent upwelling. Its intensity varies throughout the year, with maximal intensity and extension in boreal winter and spring (Lathuilière et al., 2008; Cropper et al., 2014; Romero et al., 2020; Fig. 2). The offshore transport by the upwelling filaments is considerable, and it has been estimated that during periods of intense upwelling 80 % of the shelf particular matter production is transported into the open ocean up to 400 km offshore, whereas remineralization and turbulence sustain production and enhanced transport of organic carbon to 2000 km westwards (e.g. Gabric et al., 1993; Lovecchio et al., 2017, 2018).
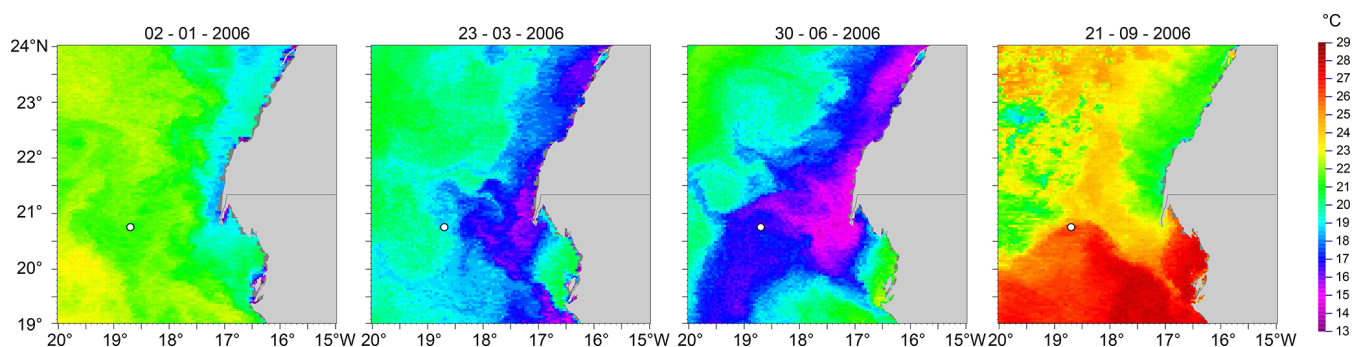
Figure 2. Temperature distribution off Cap Blanc for 4 d, each from a different season. The location of sediment trap CBeu is indicated by a white circle. Colder waters near the African coast result from upwelling. The westward extension and location of colder upwelled waters is highly variable as is upwelling. Days with strong (30 June 2006) or weak (2 January 2006) upwelling may occur any time of the year. From mid-July to November a temperature pattern similar to that of 21 September 2006 is more typical. Data are from ERDDAP, ID: nceiPH53sstn1day_Lon0360. NOAA Climate Data Record, AVHRR Pathfinder Version 5.3 L3-Collated. Data are courtesy of NCEI.

2 Material and methods

2.1 Sample collection

Particulate organic matter forming the base of this study was collected between June 2003 and March 2008 off Cape Blanc at the eutrophic mooring station CBeu (Fig. 1; Table 1). For the trap type and sampling performance, see Romero et al. (2020). Classical cone-shaped traps with a surface opening area of $0.5\,\text{m}^2$ were used (Kiel SMT 230/234; Kremling et al., 1998). Over the 5 years studied, 120 samples were collected in total. Prior to each deployment, sampling cups were poisoned with 1 mL of concentrated $HgCl_2$ per 100 mL of filtered seawater. Pure NaCl was used to increase the density in the sampling cups up to 40‰. Upon recovery, samples were stored at $4\,°C$ and wet split in the MARUM sediment trap laboratory at Bremen University, Bremen, using a rotating McLane wet splitter system. The largest swimmers, such as crustaceans, were handpicked with forceps, and remaining swimmers >1 mm were removed by carefully filtering through a 1 mm sieve prior to splitting. All flux data hereafter refer to the size fraction of <1 mm.

2.2 Lipid extraction

Lipids were extracted using ultrasonic disruptor probes with successively less polar solvent: MeOH, MeOH-DCM (1 : 1, v–v), and DCM (after Müller et al., 1998). The TLEs were dried over anhydrous Na_2SO_4 and saponified with 0.1 M KOH in 90/10 MeOH : H_2O for 2 h at $80\,°C$. For desalting, each sample was washed with distilled water and a solution of DCM : MeOH (1 : 1, vol : vol). The supernatant was removed, and the DCM : MeOH phases were rotary evaporated and later dried over anhydrous Na_2SO_4. Total lipid extracts were saponified with 6 % KOH in MeOH at $85\,°C$ for 2 h. The neutral lipid fraction was extracted with hexane and then fractionated into three polarity fractions using Bond

Elut silica gel cartridges. The first three fractions were eluted in 2 mL each of hexane, hexane : dichloromethane 1 : 2 v–v, and methanol. For the samples from the fifth deployment of the eutrophic Cap Blanc trap (CBeu5) androstanol was used as internal standard.

2.3 Lipid data acquisition

For diol analyses the polar fractions were silylated with 100 µL N,O-bis(trimethylsilyl)trifluoroacetamide (BSTFA) for 1 h at $70\,°C$. Except CBeu5 (see below), the concentrations of the different diol isomers were determined using a time-of-flight mass spectrometer (TOF-MS) LECO Pegasus III (LECO Corp., St. Joseph, MI) interfaced to an Agilent 6890 gas chromatograph (GC). The GC was equipped with a 15 m × 0.18 mm i.d. Rtx-1ms (Restek Corp., USA) column (film thickness: 0.10 µm) with an integrated 5 m guard column. A temperature-programmable cooled injection system (CIS4, Gerstel) in combination with an automated liner exchange facility (ALEX, Gerstel) and a multi-purpose autosampler (MPS 2, Gerstel) were used for sample injection. The CIS was operated in solvent vent mode (2.5 µL injection volume) and initially held at $40\,°C$ for 0.05 min and then heated at $12\,°C\,s^{-1}$ to $80\,°C$ (held 0.1 min) with the split valve open, a vent flow of $100\,\text{mL}\,\text{min}^{-1}$, and a vent time of 10 s. After the solvent vent time, the split valve was closed, and the CIS was heated at $12\,°C\,s^{-1}$ to $340\,°C$ and held for 2 min for sample transfer to the GC column. The GC oven was initially held at $60\,°C$ for 1 min and then heated at $50\,°C\,\text{min}^{-1}$ to $250\,°C$ and at $30\,°C\,\text{min}^{-1}$ to $310\,°C$ (held 2.5 min), resulting in an analysis time of 9.3 min per sample. Helium was used as a carrier gas in constant flow mode at a rate of $1.5\,\text{mL}\,\text{min}^{-1}$.

The ion source was operated at a temperature of $220\,°C$ with the GC connected to the source by means of a heated transfer line set to $280\,°C$. The pressure in the flight tube of the MS was 2.7×10^{-5} Pa. Full range mass spectra from m/z

Table 1. Deployment data of sediment trap CBeu.

Mooring	Coordinates	GeoB no. cruise	Trap depth (m)	Ocean bottom depth (m)	Sample amount	Capture duration (sample no. is days)	Sampling interval
1	20°45′ N 18°42′ W	– POS 310	1296	2714	20	1 = 10, 2–20 = 15.5	5 June 2003– 5 April 2004
2	20°45′ N 18°42′ W	9630-2 M 65-2	1296	2714	20	1–20 = 22 2–19 = 23	18 April 2004– 20 July 2005
3	20°45.5′ N 18°41.9′ W	11404-3 POS 344-1	1277	2693	20	21.5	25 July 2005– 28 September 2006
4	20°45.7′ N 18°42.4′ W	11835-2 MSM 04b	1256	2705	20	1 = 3.5 2–20 = 7.5	28 October 2006– 23 March 2007
5	20°44.9′ N 18°42.7′ W	12910-2 POS 365-2	1263	2709	38	1,2 = 6.5 3–38 = 9.5	28 March 2007– 17 March 2008

Table 2. Composition and position of the diols in the indices.

Index or diol	$1,13C_{28}$	$1,13C_{30}$	$1,15C_{30}$	$1,14C_{28}$	$1,14C_{30}$	$1,14C^*_{28:1}$	$1,14C_{30:1}$
LDI	D	D	N				
DSI				N	N	D	D
DCI				D	N		
DI$_R$			D	N	N		
DI$_W$	D	D		N	N		
CDI	D	D	D	N	N		
NDI	D	D	D	N	D	N	D

Since all proxies are indices, all diols in the numerator (N) are also in the denominator (D).

* The $1,14C_{28:1}$ diol has not been detected in the CBeu1–5 samples.

50–600 obtained under EI conditions at 70 eV were recorded at a data rate of 40 spectra s^{-1}. Processing of the TOF-MS data was accomplished with the software (ChromaTOF™) provided by the manufacturer and included automated baseline and peak finding, spectral deconvolution of overlapping chromatographic peaks, peak area calculations, and extraction of compound-specific m/z (mass-to-charge ratio) ion chromatograms.

Relative amounts of alkyl diol isomers were estimated from peak areas of specific ions resulting from α-cleavage of trimethylsilyl ethers at various mid-chain positions (de Leeuw et al., 1981) As an example, for C_{28} diols peaks were at m/z 299 (1,14 diol) and m/z 313 (1,13 diol), and for C_{30} diols peaks were at m/z 313 (1,15 diol) and m/z 327 (1,14 diols) were integrated (Rampen et al., 2008; Versteegh et al., 1997). For the diol quantification, selected reference samples containing alkyl diols in high relative amounts and without other interfering compounds (as indicated by GC/TOF-MS analyses) were additionally analysed by GC-FID on an Agilent 6890 GC equipped with a 60 m ×0.32 mm i.d. DB1-MS (Agilent J&W) column (film thickness: 0.25 µm). Samples were injected via an on-column injector. The GC oven was initially held at 60 °C for 3 min,

and then heated at 20 °C min^{-1} to 150 °C and at 6 °C min^{-1} to 320 °C (held 30 min). Helium was used as carrier gas in constant flow mode at a rate of 1 mL min^{-1}. Alkyl diols were identified by retention times, elution order, and relative abundances in comparison to the corresponding GC/TOF-MS analysis from which MS response factors for each diol were obtained. GC-FID areas of the respective diols were used for quantification by comparison to the peak area of an external n-C_{28} 1-alkanol standard. If the diol peaks consisted of a coeluting isomeric mixture, isomer proportions were quantified by their relative ratios as obtained by analysis of isomer-specific m/z ions from GC/TOF-MS. Quantified amounts of diols were then used to obtain mass-specific response factors, which allowed subsequent direct quantification of diols by GC/TOF-MS for the rest of the samples.

The diols of CBeu5 were analysed by GC-MS using an Agilent 6850 GC coupled to an Agilent 5975C MSD equipped with a fused silica capillary column (Restek Rxi-1ms; length 30 m; diameter 250 µm; film thickness 0.25 µm). The temperature programme for the oven was as follows: held at 60 °C for 3 min, increased to 150 °C at 20 °C min^{-1}, increased to 320 °C at 4 °C min^{-1}, and held at 320 °C for 15 min. Helium was used as the carrier gas, and the flow was

held constant at $1.2\,\mathrm{mL\,min^{-1}}$. The MS source was held at $230\,^{\circ}\mathrm{C}$ and the quadrupole at $150\,^{\circ}\mathrm{C}$. The electron impact ionization energy of the source was 70 eV.

Relative amounts of alkyl diol isomers were estimated from peak areas of specific ions as described above. Absolute amounts of diols were obtained by comparison to the peak area of the known amount of the internal standard androstanol (m/z 333).

2.4 Calculation of diol indices

Diol indices were calculated on the basis of relative abundances of the diol isomers.

2.4.1 Temperature proxies

The long-chain diol index is as follows (Rampen et al., 2012).

$$\mathrm{LDI} = 1, 15C_{30} / (1, 13C_{28} + 1, 13C_{30} + 1, 15C_{30}) \quad (1)$$

Sea surface temperatures have been calculated based on the following transfer functions.

$$\mathrm{SST} = (\mathrm{LDI} - 0.095) / 0.033 = 30.3\ \mathrm{LDI} - 2.88 \quad (2)$$

(Rampen et al., 2012)

$$\mathrm{SST} = (\mathrm{LDI} - 0.1082) / 0.0325 = 30.8\ \mathrm{LDI} - 3.33 \quad (3)$$

(de Bar et al., 2020)

For this study the differences between both calibrations are negligible ($<0.1\,^{\circ}\mathrm{C}$). The calibration of Rampen et al. (2012) was used.

The diol saturation index is as follows (Rampen et al., 2014a).

$$\mathrm{DSI} = (1, 14C_{28} + 1, 14C_{30})$$
$$/ (1, 14C_{28} + 1, 14C_{28:1} + 1, 14C_{30} + 1, 14C_{30:1}) \quad (4)$$

According to Rampen et al. (2014a) this index has a high correlation to temperature in *Proboscia* cultures (Rampen et al., 2009) following the relation

$$T_{\mathrm{culture}} = 40\ \mathrm{DSI} + 1.2. \quad (5)$$

The diol chain length index is as follows (Rampen et al., 2009, 2014a).

$$\mathrm{DCI} = 1, 14C_{30} / (1, 14C_{28} + 1, 14C_{30}) \quad (6)$$

Transfer functions have been published for this index on the basis of *Proboscia* diatom cultures,

$$T_{\mathrm{culture}} = 50 \cdot \mathrm{DCI} + 3.95, \quad (7)$$

on the basis of SE Atlantic core top values in relation to summer (February) SST (Rampen et al., 2009),

$$\mathrm{SST}_{\mathrm{February}} = 19.6 \cdot \mathrm{DCI} + 14.0$$
$$\left(r^2 = 0.62,\ p = 3.2 \times 10^{-6} \right), \quad (8)$$

and on the basis of the SE Atlantic data of Versteegh et al. (2000):

$$\mathrm{SST}_{\mathrm{December}} = 22.8 \cdot \mathrm{DCI} + 6.34$$
$$\left(r^2 = 0.68,\ p = 1.5 \times 10^{-4} \right). \quad (9)$$

The DSI and DCI showed high correlations to culture temperature, but these correlations were absent in a global survey relating DSI and DCI derived from core tops to SST (Rampen et al., 2014a).

2.4.2 Upwelling and upper ocean productivity proxies

The diol index of Rampen et al. (2008) is as follows.

$$\mathrm{DI_R} = (1, 14C_{28} + 1, 14C_{30})$$
$$/ (1, 14C_{28} + 1, 14C_{30} + 1, 15C_{30}) \quad (10)$$

This has been suggested as a proxy for southwest monsoon upwelling in the Arabian Sea (Rampen et al., 2008) and is also applicable to the Namibian upwelling (see Versteegh et al., 2000). The diol index of Wilmott et al. (2010) is as follows.

$$\mathrm{DI_W} = (1, 14C_{28} + 1, 14C_{30})$$
$$/ (1, 14C_{28} + 1, 14C_{30} + 1, 13C_{28} + 1, 13C_{30}) \quad (11)$$

This ratio was designed as a measure of the contribution of *Proboscia* diols relative to other diols.

The combined diol index is as follows (Rampen et al., 2014a).

$$\mathrm{CDI} = (1, 14C_{28} + 1, 14C_{30}) / (1, 13C_{28} + 1, 13C_{30}$$
$$+ 1, 14C_{28} + 1, 14C_{30} + 1, 15C_{30}) \quad (12)$$

2.4.3 Upper ocean nitrate and phosphate concentration proxies

The nutrient diol index (NDI) is as follows (Gal et al., 2018).

$$\mathrm{NDI} = (1, 14C_{28} + 1, 14C_{28:1}) / (1, 14C_{28}$$
$$+ 1, 14C_{28:1} + 1, 14C_{30} + 1, 14C_{30:1}$$
$$+ 1, 13C_{28} + 1, 13C_{30} + 1, 15C_{30}) \quad (13)$$

$$\left[\mathrm{PO_4^{3-}}\right] = (\mathrm{NDI} - 0.015) / 0.413 = 2.42\ \mathrm{NDI} - 0.0363 \quad (14)$$
$$\left[\mathrm{NO_3^{-}}\right] = (\mathrm{NDI} - 0.075) / 0.026 = 38.5\ \mathrm{NDI} - 2.88 \quad (15)$$

As may be expected, the ratio of the slopes of these transfer functions is $1:16$, the Redfield ratio (Redfield et al., 1963).

Generally, fluxes recorded in sediment traps have a logarithmic nature. As a result, linear correlations between diols are subject to bias by single high values. To overcome this bias, we based our correlations on the log-transformed diol

concentrations (Fig. S1 in the Supplement). Diol concentrations of CBeu1–4 are on average more than 1 order of magnitude (20.71 times) lower than for CBeu5 (Fig. S2 in the Supplement). Although this does not affect the diol proxy ratios, it does affect the direct comparison of diol fluxes. Concentrations of CBeu1–4 have been calculated with an external standard and by using the peak areas, response factors, injection volume, and sediment mass. In contrast, diol concentrations of CBeu5 have been calculated using peak areas, response factors, and an internal standard, and these fluxes are in good agreement with those reported from other sediment traps from high-productivity regions (Rampen et al., 2008, de Bar et al., 2019). For comparison of diol concentrations between both trap series, we multiplied the CBeu1–4 values by 20.71 to agree with those of the better-validated CBeu5 concentrations. Obviously, these new values do not represent exact concentrations, but they reduce the concentration error considerably, whereas the concentration dynamics between the individual samples remain intact (Fig. S2).

2.5   Alkenone-based $U_{37}^{K'}$ SST proxy

Lipid SST proxy data on long-chain-alkenone-based $U_{37}^{K'}$ have been determined for trap CBeu5 (material collected between 28 March 2007 and 17 March 2008). Data have been combined with those of Mollenhauer et al. (2015) for CBeu1–4.

The alkenones in the second fraction were analysed using an Agilent 5890 gas chromatograph equipped with a DB5-MS capillary column and a flame ionization detector. Alkenone identification is by relative retention times and comparison with a laboratory-internal standard sediment. The $U_{37}^{K'}$ index was calculated using the peak areas of the $C_{37:2}$ and $C_{37:3}$ alkenones (Prahl and Wakeham, 1987):

$$U_{37}^{K'} = [C_{37:2}] / ([C_{37:2}] + [C_{37:3}]).\tag{16}$$

Analytical precision based on repeated analyses of the standard sediment is ± 0.01 units of the $U_{37}^{K'}$ index. The $U_{37}^{K'}$ values were converted to temperatures using the calibration for suspended particulate matter (Conte et al., 2006):

$$SST_{UK} \ (^{\circ}C) = -0.957 + 54.293 \ U_{37}^{K'}$$
$$- 52.894\left(U_{37}^{K'}\right)^2 + 28.321\left(U_{37}^{K'}\right)^3.\tag{17}$$

The average SST_{UK} of CBeu1–4 (Mollenhauer et al., 2015) is lower than that of CBeu5 (t test for the same mean $p = 0.0014$; F test for same variance $p = 0.024$; Monte Carlo permutation, mean $p = 0.0014$, variance $p = 0.0016$ with 10^4 permutations; Epps–Singleton test for the same distribution of two univariate samples $p = 1.5 \times 10^{-6}$). Correction of this analytical discrepancy has been performed on the basis that alkenone composition reliably reflects the ambient temperature during production (Conte et al., 2006). Furthermore, we allowed for a small degree of selective degradation during transport through the water column, resulting in

slightly higher SST_{UK} (global calibration of $U_{37}^{K'}$ from suspended particulate matter (SPM) to ambient SST; Conte et al., 2006). By subtracting 0.094 $U_{37}^{K'}$ units, the CBeu5 SST_{UK} average equals that of CBeu1–4. Application of the global calibration reveals a deviation of 0.45 °C from SST_{SAT} for the entire series CBeu1–5 ($SST_{SAT} = 0.723$, $SST_{UK} + 5.56$, $\varphi = 35$ d, $r^2 = 0.60$, average 21.76 °C), and since the slope of the global calibration differs from our dataset, the reconstructed SST_{UK} shows an offset of almost $+0.8$ °C from SST_{SAT} at the lower temperatures (18 °C) and an offset of -1.9 °C at 26 °C. Logically, the alternative is that a local calibration removes this offset. For details about this correction and the local cubic calibration, we refer to the Supplement (Fig. S3 in the Supplement).

2.6   Diatom data

Diatom counting has been performed as described in Romero et al. (2020). Data for *Proboscia alata* are presented here for the first time. Although *P. indica* is a weakly silicified species and subject to dissolution already in the upper waters, the proboscis (uppermost part of the frustule) is more strongly silicified, is easily identifiable, and can be unmistakingly assigned to the corresponding species. *P. alata* is the only *Proboscia* species present in the diatom assemblage.

## 2.7   External data

2.7.1   Insolation

Solar insolation at 20° N has been obtained from https://www.pveducation.org/pvcdrom/properties-of-sunlight/calculation-of-solar-insolation (last access: 11 March 2022). This record provided insolation for each fifth day. The four most important frequency components were extracted using the sum of sinusoids model of PAST4 of the insolation, explaining that 99.994 % of its variance has been used to generate a 5-year insolation record with daily resolution for comparison with the daily SST_{SAT} record (Fig. 3).

The insolation is not a simple sinus wave. The lowest half of the insolation amplitude (7.777–10.744 W m^{-2} d^{-1}) includes 41.2 % of the year (152 d), and the highest half accounts for 58.8 % (213 d). The 10 % highest insolation (>10.447 W m^{-2} d^{-1}) occurs for 28 % (103 d) of the year, and the 10 % lowest insolation values (<08.074 W m^{-2} d^{-1}) occur at 17 % (62 d) of the year (Fig. 3a).

2.7.2   Daily sea surface temperatures

Satellite-derived SST_{SAT} values for the CBeu have been obtained through ERDDAP and are from the daily optimum interpolation (OI) AVHRR dataset (Huang et al., 2020) for 20.875° N, 18.625° W, the grid point closest to the location of CBeu and representing the square enclosed by 21° N, 18.75° W and 20.75° N, 18.5° W (Fig. 1, green square). Daily
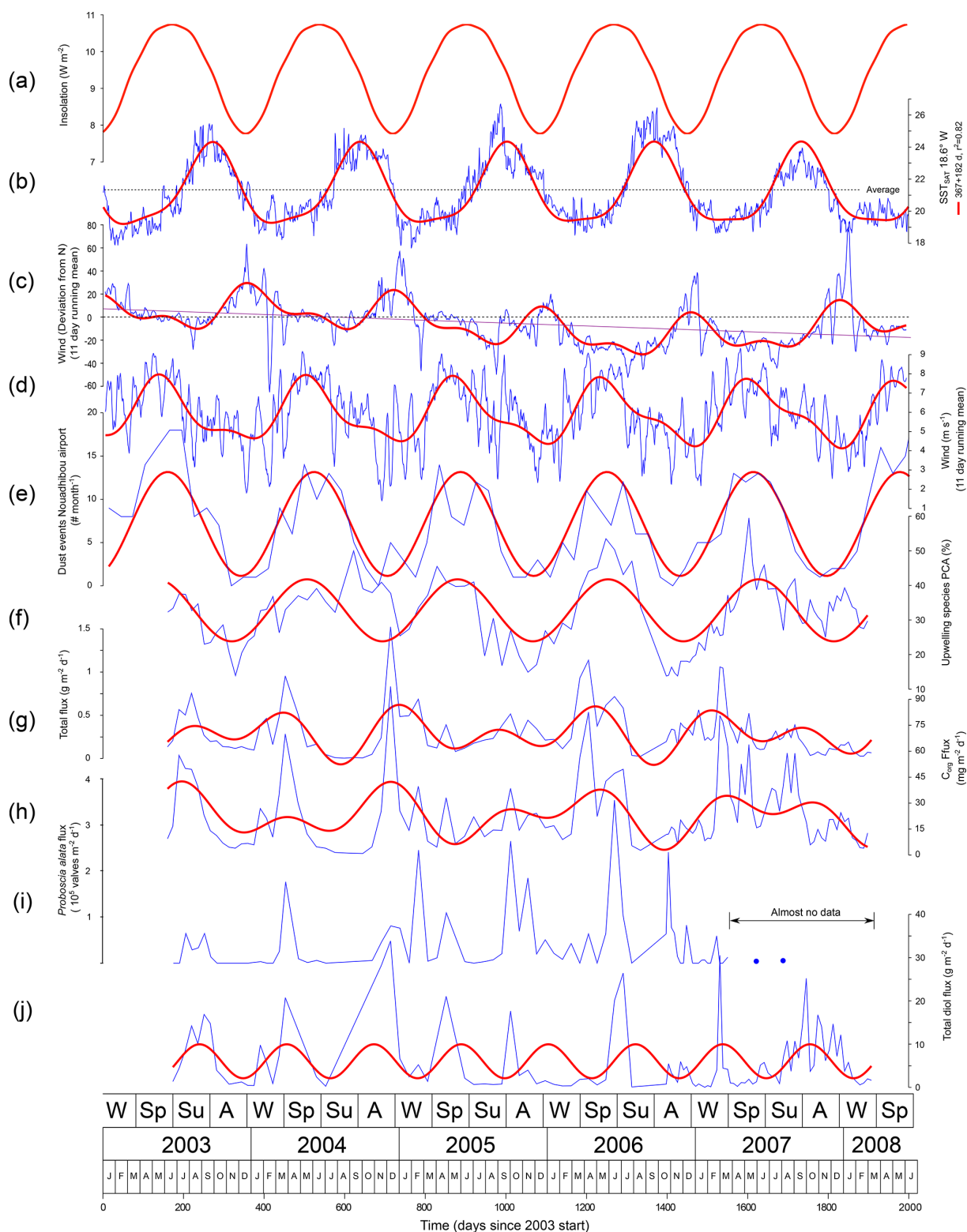
Figure 3. Variation in external variables and the total diol flux through time for CBeu1–5. Thin blue lines connect measured values (for wind parameter 11 d moving average). Thick red lines, the most important frequency components. Note that most parameters have a dominant annual cycle modulated by a semiannual cycle. The total diol flux (graph J) is dominated by a 257 d cycle. For wind direction **(c)** the scale runs from east (positive), through north (zero) to west (negative).

maps of SST_{SAT} (Fig. 2) with a 0.0417° resolution have also been obtained through ERDDAP and are from the AVHRR Pathfinder 5.3 L3C dataset with 4 km resolution (Saha et al., 2018). For each cup, the daily SST_{SAT} values have been averaged (binned) for the respective deployment time (each bin being the interval between the starting and ending dates for each cup deployment). Since it takes time for material produced in the water column to arrive in the cup, the SST_{SAT} values have also been calculated for bins shifted by 1 d ($\varphi = 1$) to 140 d ($\varphi = 140$) back in time. In this study we assume that φ is constant over time. Since the purpose of the SST proxies is to reconstruct SST, we took the φ that gave the best correlation between the binned SST_{SAT} record and the proxy-based reconstructed SST as collected by the sediment trap.

2.7.3 Monthly subsurface water temperatures, salinity, and nutrient data

Subsurface (0–600 m water depth) temperatures and salinities were obtained from the World Ocean Atlas 2018 (Locarnini et al., 2018; Zweng et al., 2019) using the statistical mean temperature on a 1° square for all decades centred at 20.5° N, 18.5° W. (Fig. 4). Monthly phosphate data for different water depths have been obtained from the World Ocean Atlas 2018 (Garcia et al., 2019) on a 5° grid point centred at 22.5° N, 17.5° W since insufficient data were available for a 1° grid point.

2.7.4 Wind direction and wind speed

Wind direction and strength are based on 3-hourly observations from Nouadhibou airport (20°56′ N, 17°2′ W; Institut Mauritanien de Recherches Océanographiques et des Pêches, Nouadhibou, Mauritania). Since these data are vector-based (direction and speed), they cannot be simply averaged (the average of $1\,h\,10\,m\,s^{-1}$ at 350° and $1\,h\,10\,m\,s^{-1}$ at 10° is $1\,h\,9.85\,m\,s^{-1}$ at 0° and not $1\,h\,10\,m\,s^{-1}$ at 180°). Therefore, the data have been decomposed into their north–south (V_n) and east–west components (V_e), averaged and converted back to directions and speeds (see Grange, 2014, and http://www.webmet.com/met_monitoring/622.html, last access: 11 March 2022). Since there is a high variability between the days, 11 d moving averages have been used to reduce this high-frequency contribution (Fig. 3). Furthermore, the deviation from north is presented ($-90°$ is west, $+90°$ east) rather than the full 360° scale.

2.7.5 Dust events

The dust data (Fig. 3) represent the monthly number of dust events as represented in the synoptic weather data recorded at Nouadhibou Airport (20°56′ N, 17°2′ W) and have been obtained from the Institut Mauritanien de Recherches Océanographiques et des Pêches, Nouadhibou, Mauritania (Romero et al., 2020) (Fig. 3f).

2.8 Statistics

Statistical analyses have been performed with the software package PAST4.0.4 (Hammer et al., 2001) and with R packages "grDevices", "stats", "EnvStats", "methods", and "car". Phase shifts reported between proxy records and SST_{SAT} represent the phase for which the correlation is highest. Phases are represented by φ and wavelengths by λ.

3 Results

3.1 Environmental data

3.1.1 Daily sea surface temperatures

Daily SST_{SAT} values are above average (21.3 °C) from July to December (5 months) and low and relatively constant from December to July (7 months Fig. 3b). The maximum temperature is reached on 30 September (day 273, just over 6 months after the minimum). The daily maps of SST_{SAT} for the region show that in contrast to previous years extensive upwelling continues, largely keeping away the relatively warm southern waters (such as depicted in Fig. 2d) from July to December 2007 so that the SST_{SAT} values are considerably reduced for this period (Fig. 3b). As a result, the annual (March 2007 to March 2008) SST_{SAT} is 0.6 °C lower than March 2003 to March 2007 ($p = 2.1 \times 10^{-7}$).

The records of binned SST_{SAT} averages (representing the averaged SST for the deployment period of each cup) varies depending on the assumed phase shift (φ) between the genesis of a signal at the sea surface and its arrival in the cup of the sediment trap. Minima lay between 17.9–18.4 °C, maxima between 26.2–27.2 °C, and annual amplitudes between 7.8–8.9 °C.

3.1.2 Monthly subsurface water temperatures, salinity, and nutrients

The temperature–salinity diagram for the upper 600 m (Fig. 4) shows for November–December a predominantly South Atlantic Central Water (SACW) signature with relatively low salinities for a given temperature (or high temperatures for a given salinity). From January, the contribution of North Atlantic Central Waters (NACW) increases. From March to June the upper 80 m shows admixture of cool, low-salinity waters (but absent in April) so that despite increasing insolation the SST stays below 19 °C for this period.

For the upper 40 m a decrease in PO_4^{3-} occurs from January with a minimum in April (Fig. 4). In May, June, and July the values are back at their February–March values and return to the April minimum from August to October, coinciding with the summer stratification. From September, values increase to the January maximum. Below 40 m, the highest PO_4^{3-} concentrations are not in January but in December.
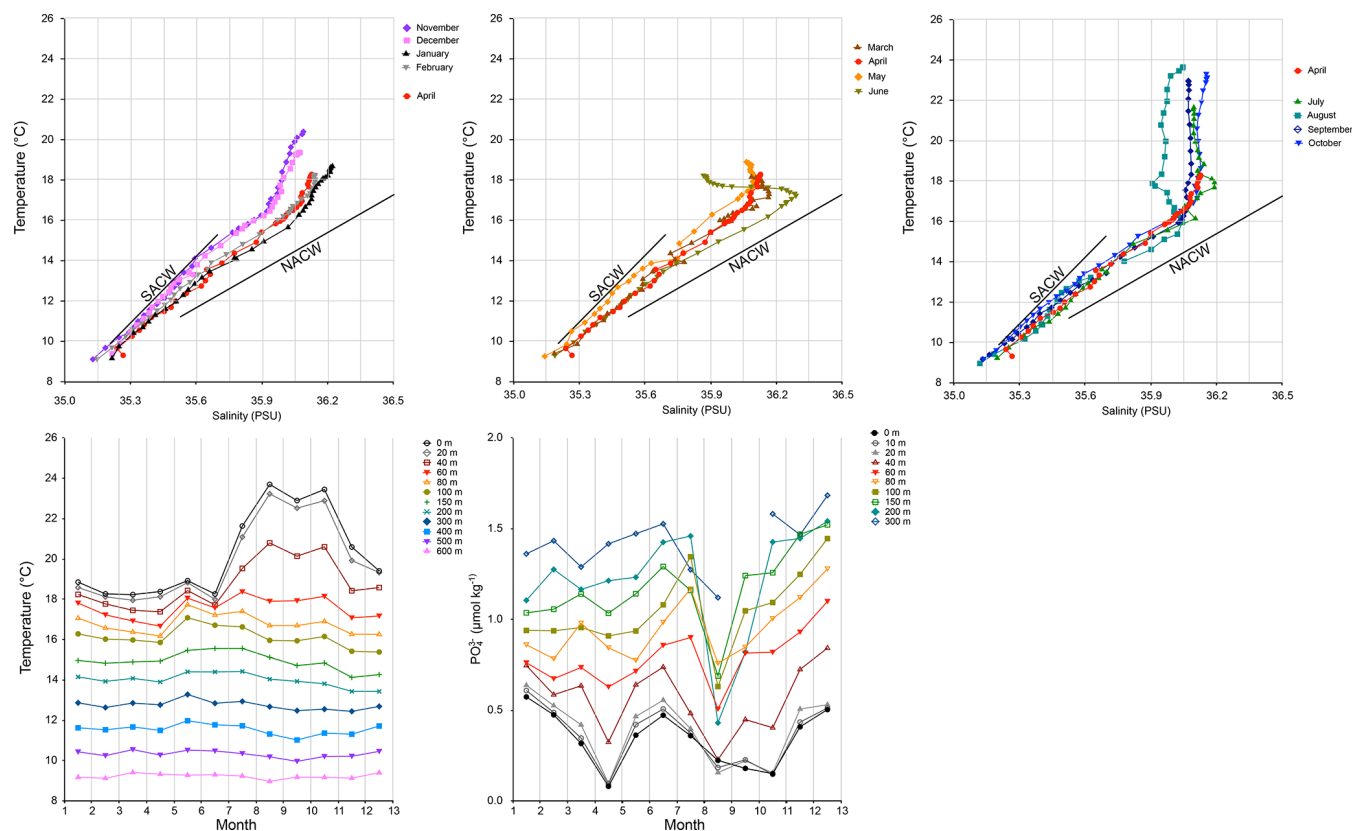
Figure 4. Oceanographic data from the World Ocean Atlas 2018 (WOA). The upper three panels show temperature–salinity diagrams for each month for the 1° square centred at 20.5° N, 18.5° W. Solid lines represent the North Atlantic Central Water (NACW) and the South Atlantic Central Water (SACW) (Locarini et al., 2018). The lower left panel shows water temperatures for different depths in the same 1° square (Zweng et al., 2019). The lower right panel shows monthly PO_4^{3-} concentrations against depth for the 5° square centred at 22.5° N, 17.5° W (Garcia et al., 2019).

Values stay more or less constant from January to May. In June and July they increase and sharply fall to a minimum in August. In September and October values are back to June values and they further increase in November and December.

3.1.3 Wind direction and wind speed

From 2003 to 2008 the 11 d averaged wind blows 87 % of the time from NW to NE (36° E–21° W) and 52 % of the time from NNW to NNE (17° E–7° W). Most easterly directions occur in a relatively short period from November to February, when wind speed is at its lowest on average (Fig. 3d). This phase with more easterly winds was poorly developed in 2005/2006. This is followed by a period of high wind speeds from March to July with winds more or less constant from the north (or NW in 2006 and 2007; Fig. 3e). A third period, from June to November, has the same overall wind as the preceding period but intercalates more westward outbreaks, and wind speed tends to be lower. Over the investigated period there is a westward trend ($D = -0.0124$ d -7.49, whereby D is the direction in degrees from W and d is Julian day since 1 January 2003; $r^2 = 0.14$; $p = 9.45 \times 10^{-9}$ $n = 1989$). This

implies that at the beginning of 2003 the average wind direction is 7.5° N, and by the end of the study period (after 2000 d) this is 17.4° W. This effect is predominantly due to the years 2007 and 2008 for which from the beginning of May to the end of October the wind has a more westerly direction than during this period in the preceding years (Fig. 3). Frequency analysis shows, apart from this long-term trend, an annual cycle (363 d) and a 6-month cycle (184.6 d) with its most eastern direction at 10 December.

The 11 d averaged wind speed varies between 1 and 9 m s^{-1} and shows no trend (slope 1.4×10^{-4}). Frequency analysis shows an annual cycle (371 d) and a 6-month cycle (181 d). The phase of the cycle is 45 d (from 1 January) with the maximum wind speed $1/4\pi$ later ($45 + 93 = 138$ d), which is 18 May.

3.1.4 Dust events

The dust record shows a strong seasonal cycle ($\varphi = 55.33$ d, $\lambda = 363.2$ d), and the abundance of dust events lags wind speed by 10 d.

3.2 Sediment trap mass fluxes and upwelling species abundance

The relative abundance of upwelling species (% Upw) shows a clear seasonal cycle and lags wind speed by 21 d ($r^2 = 0.29$, $p = 3.5 \times 10^{-9}$) and conversely dust event frequency by 11 d. The % Upw species correlates well with the SST_{SAT} (negative $r^2 = 0.53$, $\varphi = 76$, $p < 2.5 \times 10^{-20}$; positive $r^2 = 0.40$, $\varphi = -119$, $p < 2 \times 10^{14}$). Total mass flux maxima occur in concentrated intervals of which the timing and amplitude may differ between the years. Total mass fluxes, and fluxes of carbonate, C_{org}, biogenic silica, and the lithogenic component all closely correlate and are synchronous (e.g. C_{org} flux = $0.065 \cdot$ total flux $+4.20$ $r^2 = 0.74$; Fig. 3g, h) (Romero et al., 2020). Maxima may occur at any time but are most frequent in late winter from February to March. In 2003 and 2008 a spring maximum is absent. The years 2005 and 2007 have maxima in late summer. Both the amplitude of the total mass and flux maxima differ between the years. In 2005 a series of small flux maxima occur, but a large maximum is missing (Fig. 3). As a result of this irregular timing of total mass flux maxima, the most important frequency component is not the annual cycle but a cycle with a length of 257 d ($r^2 = 0.17$, $p = 4.04 \times 10^{-6}$).

3.3 Diol fluxes

The $1,14C_{28}$, $1,14C_{30}$, and $1,15C_{30}$ diols could be detected in 105 of the 120 cups. For several of these cups other diols were below the detection limit with the $1,14C_{30:1}$ detected least, in only 61 cups. Diol flux maxima coincide with total mass flux maxima (Fig. 3), albeit not every total mass flux maximum is accompanied by a diol flux maximum. The wavelength of the most important diol flux frequency component is 216 d ($r^2 = 0.14$, $p < 3.4 \times 10^{-5}$). Sorting the samples in order of increasing (or decreasing) flux shows that the flux amplitude changes logarithmically with sample rank number ($r^2 = 0.99$). For the LDI-relevant diols the flux increases (decreases) by factor of 2 about every 10 samples (Fig. S4 in the Supplement). Fluxes of individual diols show a cluster of high correlations consisting of the $1,13C_{30}$ diol and both 1,15 diols ($r^2 > 0.75$). The $1,13C_{28}$ diol correlates best with the $1,13C_{30}$ diol and ($r^2 > 0.75$) less with the 1,15 diols ($r^2 > 0.50$) and even less with the 1,14 diols. The 1,14 diols correlate best with each other ($r^2 > 0.83$), whereby the $1,14C_{28}$ diol correlates less with the other diols than the $1,14C_{30}$ diol. The $1,14C_{30:1}$ diol does not show strong correlations with the other diols. It correlates best with the $1,14C_{30}$ diol and second best with the 1,15 diols. We relate this absence of strong correlations with the $1,14C_{30:1}$ diol to its low concentrations, which intrinsically have a large error bar and are accompanied by occurrences below the detection limit. Excluding the $1,14C_{30:1}$ diol, the $1,13C_{28}$ and $1,14C_{28}$ diols correlate least. Thus, overall, the 14 and 15 diols correlate least ($r^2 = 0.45$), and the 13 diols

are intermediate but have a higher correlation with the 15 diols ($r^2 = 0.79$) than the 14 diols ($r^2 = 0.48$). We were unable to detect 1,12 diols.

3.4 Diol ratios and indices

The NDI, DI_W, DI_R, CDI, and to a lesser extent DSI covary to a considerable extent ($r^2 > 0.46$; Table 4, Fig. 5). The reason for this is that all have the $1,14C_{28}$ diol in the numerator, which is the most abundant diol in the record (40 % of the diol flux). Furthermore, all but the NDI also have the covarying $1,14C_{30}$ (Table 3) in the numerator (second in abundance with 24 % of the diol flux). Finally, in the denominator these indices all have 1,13 and/or 1,15 diols. The dominance of the $1,14C_{28}$ and $1,14C_{30}$ diols is also illustrated by the strong anticorrelation of the DCI and NDI, which have both diols in opposite positions of the fraction. Due to their annual cyclicity, statistically the diol indices correlate to environment with two maxima of opposite sign and about 181 d apart (half cycle). For some indices the causal relation to environment is not clear a priori. In the case of a negative correlation with environment, the correlation is positive if shifted by a half cycle, but this is also true for the unshifted reciprocal of the proxy. Below, we often provide both negative correlations and their phases with environmental variables without further interpretation, which will be added in the discussion.

3.4.1 Temperature proxies LDI, DSI, and DCI

The SST_{LDI} maximum of 26.7 °C is 1.1 °C above the binned SST_{SAT} maximum, which, considering the error bars, is a reasonable approximation (25.6 °C at $\varphi = 41$ d, Fig. 6). However, the minimum of 10.9 °C is 7.7 °C lower than the lowest binned SST_{SAT} value (18.6 °C at $\varphi = 41$). In total there are four values below this lowest binned SST_{SAT}, and they occur in July 2003, July 2006, and March 2007, all in cup series CBeu1–4. A simple box plot shows that these values are outside the notches, which indicate approximately the 95 % confidence interval (Fig. 7). The Rosner test for identifying multiple outliers (from R package EnvStats) identifies the lowest four values (< 18 °C), as outliers ($p < 0.006$ and for the lowest value < 11 °C $p < 0.0001$). Cross-correlation plots (Fig. 8) of the log-transformed diol fluxes show that the anomalies are most pronounced in the $1,13C_{30}$ diol relative to each of the 1,15 diols and do not correlate with the flux amplitude. For several samples no 1,13 diols could be detected. This lack of information automatically results in LDI values of 1, translating into 27.42 °C, which is unrealistic in this setting. For these reasons, such data points have been omitted.

A linear correlation of LDI to binned SST_{SAT} explains 17 % of the variance ($\varphi = 41$, $p = 1.4 \times 10^{-4}$, $n = 82$, Table 4). The linear correlation of SST_{LDI} to binned SST_{SAT} also explains only 17 % of the SST_{SAT} variance ($\varphi = 38$, $p = 1.2 \times 10^{-4}$). The integrated production temperature is 23.6 °C (with the outliers 22.9 °C).

Table 3. Correlations of diol concentrations and their natural logarithms for CBeu1–5.

	Lipid	$1,13C_{28}$	$1,14C_{28}$	$1,13C_{30}$	$1,14C_{30:1}$	$1,14C_{30}$	$1,15C_{30}$	$1,15C_{32}$
	$1,13C_{28}$	–	*0.35*	*0.59*	*0.01*	*0.31*	*0.44*	*0.58*
	$1,14C_{28}$	0.42	–	*0.14*	*0.01*	*0.69*	*0.11*	*0.20*
	$1,13C_{30}$	**0.75**	0.29	–	*0.01*	*0.19*	*0.70*	**0.81**
Natural	$1,14C_{30:1}$	0.18	0.17	0.14	–	*0.20*	*0.00*	*0.01*
logarithm	$1,14C_{30}$	0.58	**0.83**	0.50	0.33	–	*0.12*	*0.20*
correlations* (r^2)	$1,15C_{30}$	0.62	0.36	**0.82**	0.14	0.51	–	**0.84**
	$1,15C_{32}$	0.70	0.34	**0.84**	0.17	0.51	**0.85**	–
	1,13 vs 1,14	0.48						
	1,13 vs 1,15	**0.79**						
	1,14 vs 1,15	0.45						

Column header spanning: Linear correlations* (r^2)

Outliers: $1,13C_{28}$ and $1,13C_{30}$ of CBeu1–4, CBeu3–18, CBeu4–18, and CBeu4–19 are excluded. Bold typeface is correlations >0.74.
* Linear correlations in italics.

Table 4. Correlations (r^2) between diol proxies and environment.

	DI_W	DI_R	CDI	NDI	DCI	DSI	LDI
DI_R	**0.65**						
CDI	**0.69**	**1.00**					
NDI	**0.49**	**0.46**	**0.48**				
DCI	*0.32*	*0.15*	*0.16*	*0.74*			
DSI	0.080	*0.0004*	0.0005	**0.67**	*0.46*		
LDI	*0.036*	*0.27*	*0.24*	*0.029*	*0.0003*	**0.09**	
ln *P. alata* flux	**0.12**	**0.29**	**0.29**	0.000	0.051	*0.019*	
Total flux	0.011	0.024	0.021	0.001	*0.017*	*0.013*	
% Upw spp.	*0.20*	*0.07*	**0.09**	*0.38*	*0.42*	*0.39*	*0.02*
Wind speed	*0.19 φ 79*	*0.11 φ 79*	**0.093 φ 35**	**0.28 φ 32**	**0.29 φ 30**	**0.24 φ 21**	
SST (lead)	*0.23φ − 69*	*0.10φ − 69*	*0.13φ − 69*	**0.38φ − 77**	**0.29 φ − 77**	*0.42φ − 124*	(0.21φ140)
SST (lag)	**0.27 φ 94**	**0.13 φ 105**	**0.15φ 104**	**0.34 φ 102**	*0.35φ 117*	**0.25 φ 76**	**0.17 φ 41**

Correlations with $p<0.05$ are in bold, and negative relations are in italics. LDI outliers are not included.

The DCI correlates significantly with SST_{SAT} (negative correlation at $\varphi = 117$, $r^2 = 0.35$, $p < 4 \times 10^{-11}$ positive correlation at $\varphi = -77$, $r^2 = 0.29$, $p < 2.8 \times 10^{-9}$; Fig. 6). As such SST_{SAT} could be reconstructed from DCI using the positive correlation

$$SST_{SAT} = 6.45 \ DCI + 18.4 \qquad (18)$$

(95 % conf.: slope 4.31 to 8.68, intercept 17.5 to 19.2) or the negative correlation

$$SST_{SAT} = -8.13 \ DCI + 16.79 \qquad (19)$$

(95 % conf.: slope −9.99 to −6.12, intercept 23.9 to 25.8)
The DCI lags wind strength ($\varphi = 30$ positive correlation, $r^2 = 0.29$, $p < 5.5 \times 10^{-9}$). The DCI shares most variance with the NDI (74 %) with a negative correlation.

The DSI correlates strongly with the NDI and DCI (Table 4). The positive correlation with SST_{SAT} ($r^2 = 0.25$,

$\varphi = 77$, $p = 5.7 \times 10^{-5}$) is much lower than the negative correlation ($r^2 = 0.42$, $\varphi = -124$, $p = 3.4 \times 10^{-8}$). For a considerable number of samples no unsaturated diols could be detected, in which case the DSI is not defined and 1. However, if the response of the combined 1,14 diols is 100 times higher than the detection limit of the $1,14C_{30:1}$ diol, the DSI has to be >0.99, otherwise it would have been detected. If the response is less than a factor of 100, it may be that the DSI was <0.99 but the diol concentrations were in general too low to detect the $1,14C_{30:1}$. Taking also into account the different response factors of the diols, 11 samples without detected unsaturated diols for which the DSI could be >0.99 were identified. Statistical analyses including these samples showed mostly slightly lower correlations compared to the dataset without them, and we present the results with these 11 samples excluded from the DSI.
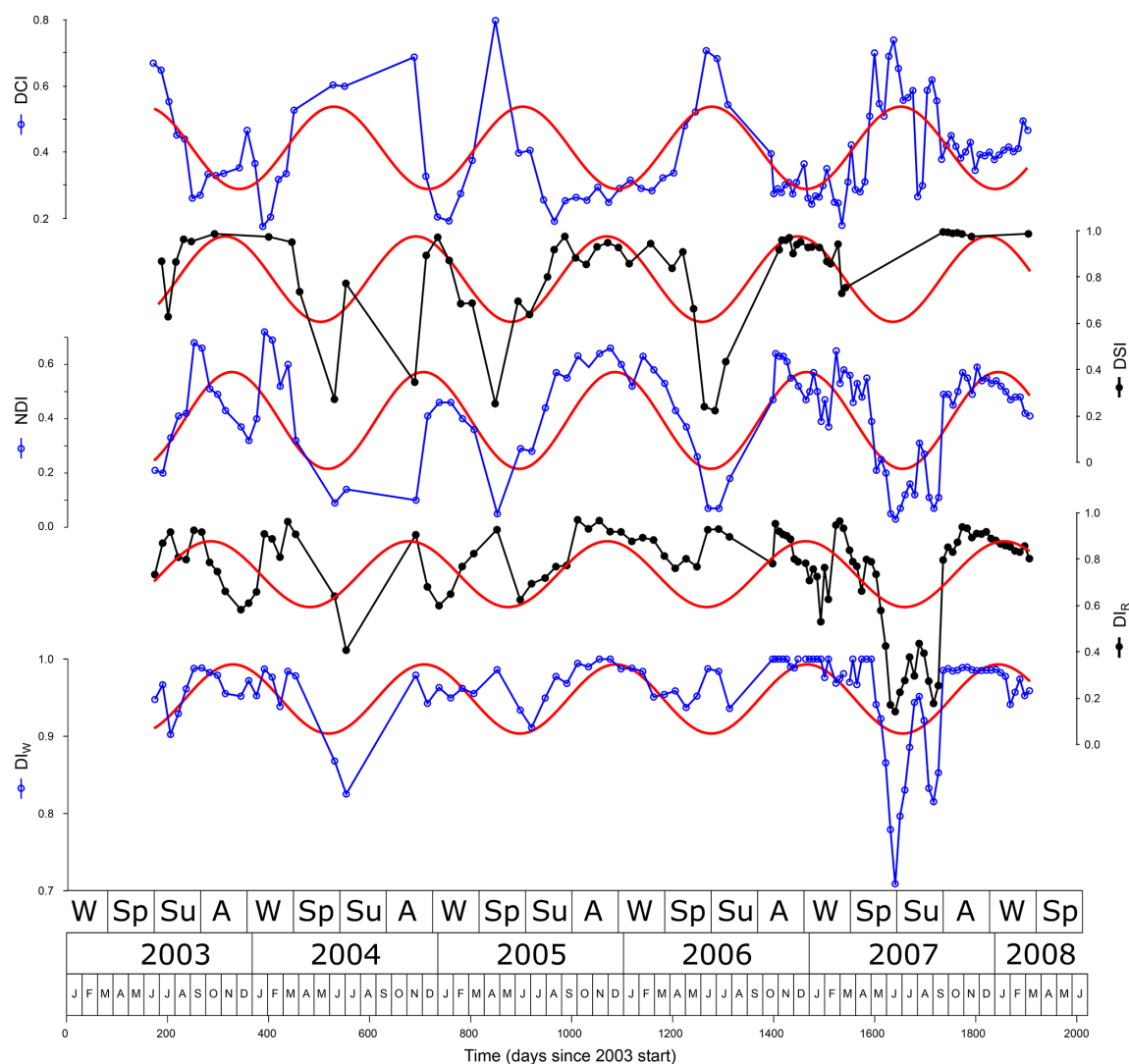
Figure 5. Diol proxies and their main (annual) frequency component. Note the close similarities between the diol proxies and the DCI behaving opposite to the others.

### 3.4.2 Upwelling and upper ocean productivity proxies DI$_R$, DI$_W$, and CDI

The DI$_R$, as a proxy for the *Proboscia* contribution, correlates significantly with the ln *P. alata* flux ($r^2 = 0.29$, $p = 1.6 \times 10^{-4}$) but not with the total mass flux or its logarithm (Fig. 9).

The DI$_W$ as a proxy for upwelling correlates significantly with the ln *P. alata* flux ($r^2 = 0.12$, $p = 0.024$) but not with the total mass flux ($r^2 = 0.011$, $p = 0.25$). The correlation of the DI$_W$ with the LDI is negative low ($r^2 = 0.04$) and just not significant ($p = 0.09$), for the DI$_R$ and LDI the correlation is also negative but much higher ($r^2 = 0.24$, $p = 6.3 \times 10^{-7}$). Both the DI$_R$ and DI$_W$ show a negative correlation with wind strength, which is best at $\varphi = 79$ (Table 4).

The combined diol index (CDI) (Rampen et al., 2014a) is almost identical to the DI$_R$ ($r^2 = 0.995$) and therefore has not been evaluated separately.

3.4.3 Upper ocean nitrate and phosphate concentration proxy NDI

The NDI shares about half its variance with the CDI, DI$_W$, and DI$_R$, even higher with the DCI (74 %) and DSI (67 %). The NDI shows correlation with neither *P. alata* flux ($r^2 = 0.005$, $p = 0.6$) nor the total mass flux ($r^2 = 0.0014$, $p = 0.7$) but correlates well ($r^2 = 0.38$, $p = 4.1 \times 10^{-12}$) with the relative abundance of upwelling-indicating species (% Upw) in the samples.
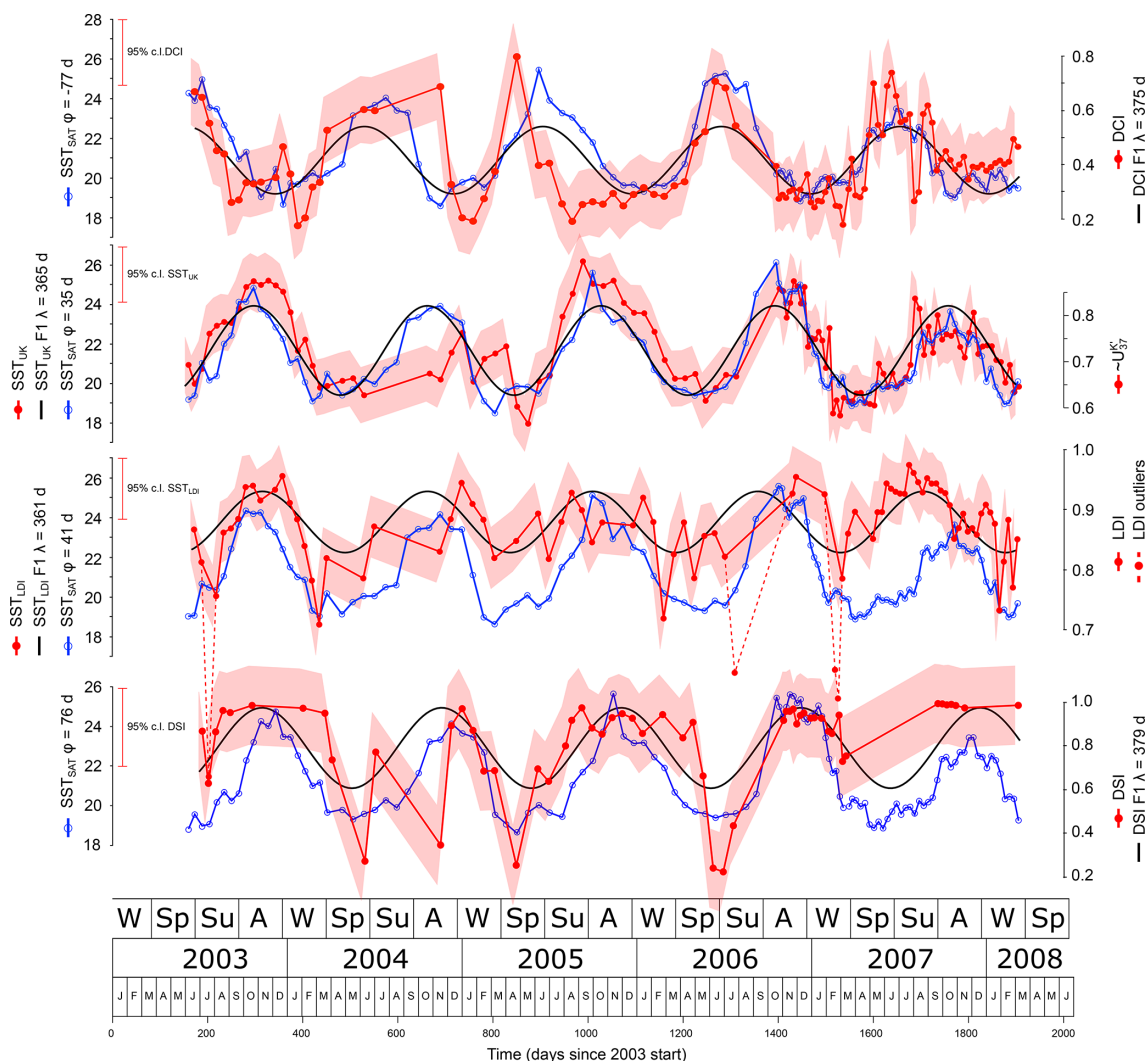
Figure 6. Proxy-derived SST (red, filled circles), their annual frequency component (F1, black), and satellite-derived SST_{SAT} (blue, empty circles). The phase shifts of the SST_{SAT} are such that correlation with the proxy-derived SST is highest. Corresponding proxy values are indicated on the right side of the panels. Shaded red areas show the 95 % confidence range.

3.5 Alkenone-based $U_{37}^{K'}$ and SST_{UK}

The SST_{UK} values are 18.0–26.1 °C and best fit to SST_{SAT} if SST_{UK} at $\varphi = 35$ d (Fig. 6). For this phase lag the binned SST_{SAT} values are 18.5–26.1 °C, and the SST_{UK} record thus has about the same amplitude extending 0.5 °C below the minimum and equalling the maximum SST_{SAT}. The regressions of $U_{37}^{K'}$ and SST_{UK} to binned SST_{SAT} do not differ much in the explained variance and phase (φ 35 d, $r^2 = 0.59$ vs. 0.60). The flux-corrected SST_{UK} for CBeu1–5 prior to correction is 21.54. After correction it is 21.14 °C, which is only 0.23 °C lower than the SST_{SAT} for the same period (21.37$\varphi = 35$) and well within the standard error of the method (1.2 °C) (Conte et al., 2006).

4 Discussion

4.1 Water temperatures during the sampling period

During the entire record, SST_{SAT} values tend to remain relatively constant for periods of 1 to 3 weeks with rapid shifts of 1–2 °C between them (Fig. 3). During summer these shifts tend to be larger, and they may be up to 4.5 °C within a week at the transitions between summer and winter (in 2004). The duration of these 1–3-week periods of stable temperatures is similar to the deployment of individual sediment trap cups (8–24 d). As a result, these periods are partly reflected by, and consistent features of, the binned SST_{SAT} record. This is much more apparent after November 2006 when the cup deployment is systematically less than 10 d and close to the duration of the shorter-term events of the system.
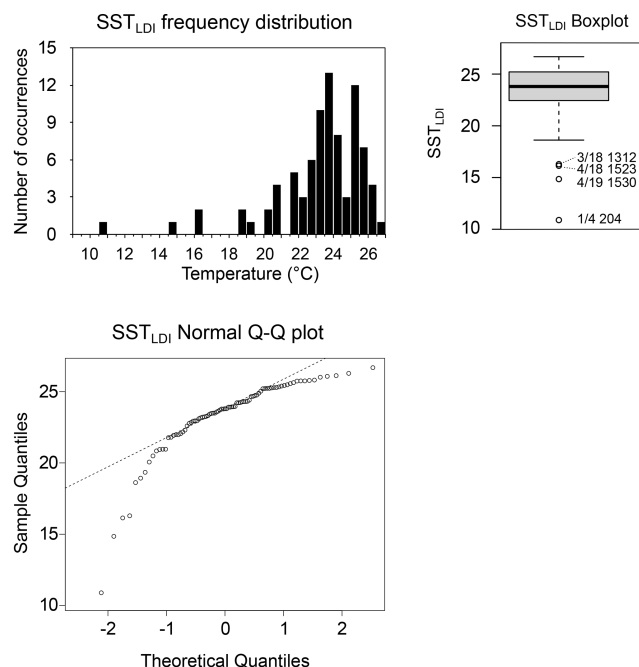
Figure 7. Statistics of the SST_{LDI} values identifying the four values below $16\,°C$ as outliers. **(a)** Frequency distribution. **(b)** Boxplot with outliers indicated with trap deployment number and the cup number of that trap separated by a slash and followed by the day (since the start of 2003) the cup was halfway through its deployment. **(c)** Q–Q plot, with the dotted line representing the expected values for a normally distributed dataset.

This demonstrates that to capture the system dynamics, these shorter deployment times are the preferred mode of operation, if not a requirement.

The SST_{SAT} does not simply follow the insolation curve, but a substantial rise in temperature only starts from the beginning of June, only a few weeks before the insolation maximum. We attribute the delay to maximum intensity of the trade winds during late winter and spring, intensifying upwelling and pumping cool, low-salinity, and nutrient-rich SACW waters to the surface along the coast and subsequently spreading these westward over the trap site. Wind speeds are strongly reduced, and upwelling is at a minimum for July to October, enabling the surface waters to strongly increase in temperature, except for 2007 when upwelling reduces much less and summer temperatures stay relatively low. The temperature gradient is always small for the upper 20 m, the permanently mixed layer.

The most prominent feature of the monthly water temperature profiles is the strong annual cycle at the sea surface, which becomes smaller with increasing depth. In the upper 100 m the relatively short distances between the temperature profiles for different depths (the strength of the temperature gradient) are clearly smaller from January to June compared to the rest of the year. We attribute this to mixing and upwelling. This seems to be most intense in May and June. In

May, elevated temperatures up to 400 m depth indicate this, and in June the upwelling and mixing result in SSTs that are even lower than the preceding months, despite stronger solar insolation. We also observe that the highest temperatures at depth (80–200 m) lead the SST by about 3 months (Fig. 4), which in the case of temperature proxies generated at these depths could lead to proxy-derived temperature records leading SST.

4.2 The annual cycle, wind, dust, SST, and upwelling

All environmental parameters investigated show a dominant annual cycle modulated by a semi-annual component. This is also true for most of the proxy records. This implies that a significant correlation of a proxy parameter to an environmental variable, with a given phase shift, has a high chance to also provide significant correlations with other environmental parameters, albeit with different phase relations. Although this is no problem for proxy records with a known causal relation with environment, such as the $U_{37}^{K'}$ with temperature, this becomes a problem for proxies where this relation is less clear. First, it is not clear which environmental parameter is the forcing factor since if one parameter shows a significant correlation the others will as well. Second, the phase relation is unclear since two correlation maxima occur each environmental cycle albeit with opposite sign. Additional arguments, e.g. from the data structure and/or functioning of the system, are needed to decide which proxy–environment relation is most likely to be causal. In our system, off Cap Blanc, the modulation of the semi-annual frequency component causes asymmetry in the cycles of the environmental variables (Fig. 3). As a result, the best correlation and anti-correlation are unequal, and their phases are not a half cycle apart. Comparison of wind speeds and SST_{SAT} in this region shows that both have a short period of high values, followed by a relatively long period of low values. If proxy records follow environmental change closely, they should also display this asymmetry in the annual cycle. High wind speeds in late winter and spring drive upwelling, preventing SST_{SAT} from increasing with solar insolation so that only when wind ceases by the beginning of June can SST_{SAT} rapidly rise. This results in maximum wind speed leading maximum SST by $122\,d$ (based on 11 d means, $r^2 = 0.38$) and minimum SST leading maximum wind speed by $91\,d$ ($r^2 = 0.37$). The asymmetry in the annual cycle thus leads to an alternation of $122 + 91 = 213\,d$ difference between correlation optima, followed by a $365 - 213 = 152\,d$ difference between the next correlation optima. We expect to see this asymmetry also in the other proxy records. The frequency of dust events lags wind speed by $10\,d$ so that most events occur during the period of most active upwelling. Due to this small phase difference in relation to the generally 2 to 3 times longer sample frequency of the sediment traps, it is impossible to separate the effects of upwelling and dust input on the export flux, species, and lipid composition. Since wind speed is driving
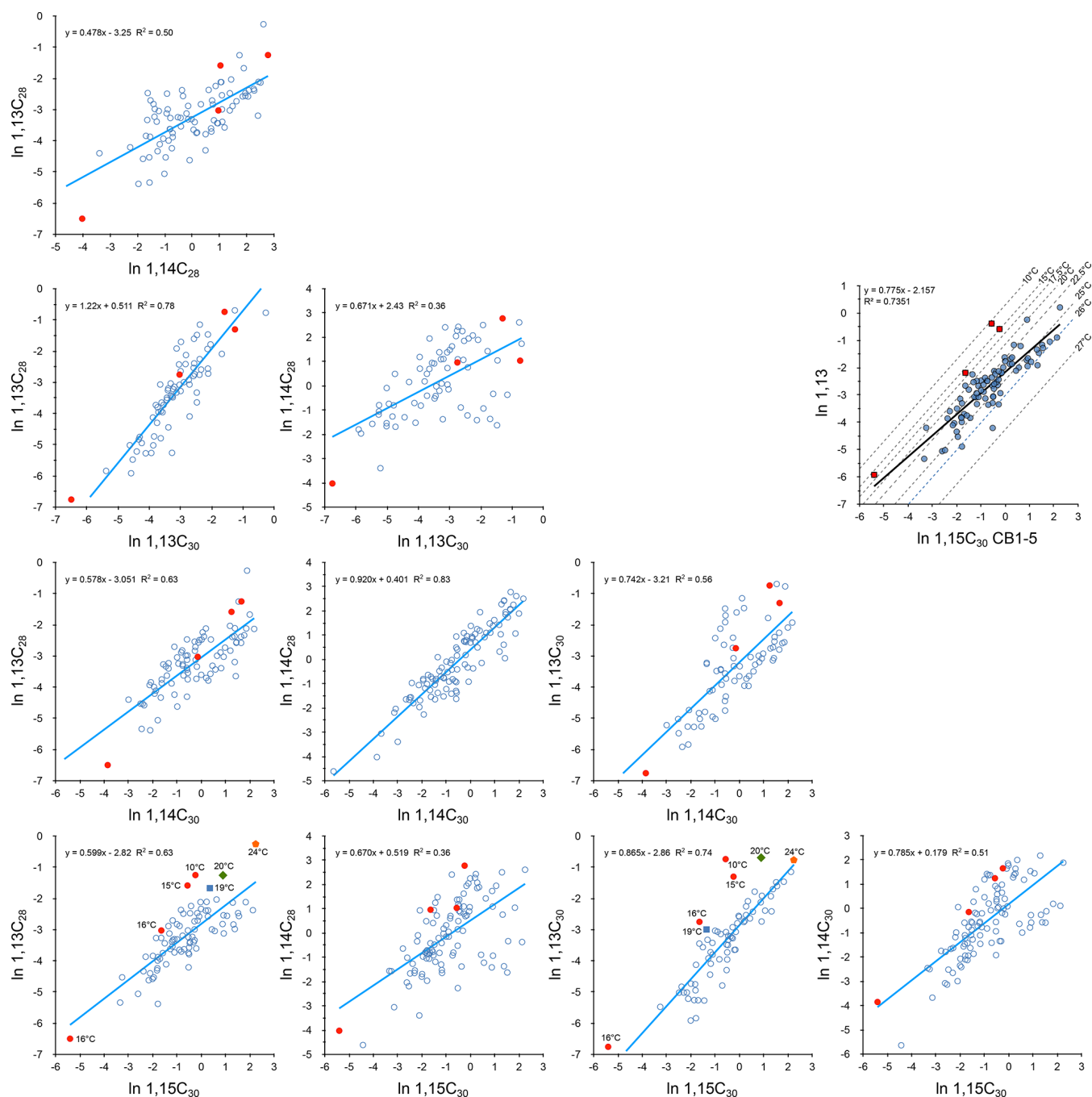
Figure 8. Cross plots of log-transformed diol fluxes ($\mu g\,m^{-2}\,d^{-1}$) with 1,13 diol values for samples providing SST_{LDI} values below $18\,°C$ in solid red. These values have not been included for obtaining the (blue) regression lines. In $1,13 \times 1,15$ diol plots other extreme points are indicated by a blue square ($19\,°C$), green diamond ($20\,°C$), and orange pentagram ($24\,°C$). In the upper right plot, the diols involved in the LDI ($1,15C_{30}$ and combined 1,13 diols) are provided. The dotted lines represent isotherms for the transfer function of Rampen et al. (2012). The regression line shows how the (log-transformed) composition of the diols involved in the LDI relates to temperature (excluding the outliers indicated by red squares).
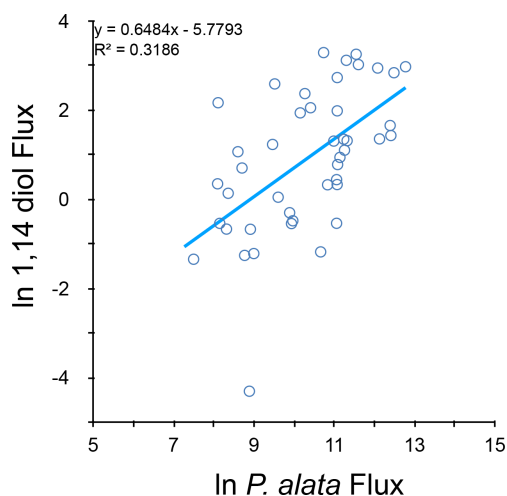
Figure 9. Correlation of natural logarithms of 1,14 diol fluxes ($\mu g\, m^{-2}\, d^{-1}$) and diatom *Proboscia alata* fluxes (valves $m^{-2}\, d^{-1}$).

both upwelling and dust event frequency, only relations to wind speed are further considered.

4.3 Diol fluxes

Diol flux maxima, like total flux maxima, may occur in any season, and, therefore, the record is not dominated by an annual cycle (Fig. 10). Whereas all diol maxima occur during total flux maxima, the opposite is not true. Apparently, flux maxima may follow from different environmental configurations, whereby some are accompanied by high diol export. An obvious hypothesis in this region would be that both productivity and dust events may induce high export production and that dust events do not necessarily occur when diol concentrations are high. Unfortunately, we do not have sufficient data to support this hypothesis. Correlations between fluxes of individual diols show that the 1,14 and 1,15 diols correlate least, whereas the 1,13 diols are intermediate but correlate better to the 1,15 diols. Indeed, flux maxima of 1,14 diols are partly independent of those of 1,15 and 1,13 diols. This supports earlier work suggesting different sources for 1,15 and 1,14 diols (e.g. Rampen et al., 2007; Gal et al., 2021), whereby the 1,13 diols may be derived from both sources. The logarithmic relation between the diol flux reached and its frequency (many low fluxes, few very high) is important for the diol composition and diol proxy values integrated over timescales longer than a cup-to-cup basis. The more uneven the distribution, the more influence a few large fluxes have on the total value. In our case, the average difference between a given flux and next largest flux is about 6.5 %, so that on average the 10th largest flux still has half the influence of the largest one (see also Sect. 4.5).

4.4 Diol-based temperature proxies LDI, DSI, and DCI

The LDI uses the underlying assumption that the percentages of 1,13 diols (relative to the 1,15C_{30} diol) decrease with temperature. For the SST_{LDI} outliers (values below 18 °C), we could not find any analytical explanation. These outliers arise from excess production of both 1,13 diols. The occurrence of these anomalies suggests that this excess production is unrelated to temperature. We observe that all three events with excess 1,13 diols (and very low LDI values) occur during total flux maxima (compare Figs. 5, 9), and as such we speculatively suggest that factors leading to elevated export productivity play a role. However, also with the outliers omitted, we observe a poor relationship between LDI and SST_{SAT} and a phase lag of 41 d ($r^2 = 0.17$) but still a significant seasonal cycle ($\lambda = 347$ d, $r^2 = 0.36$, $p = 1.2 \times 10^{-10}$). This contrasts with trap studies from the equatorial Atlantic, Mozambique Channel, and to a lesser extent the Cariaco Basin where a general absence of a seasonal cycle in the LDI has been observed (de Bar et al., 2019). The SST_{LDI} integrated production temperature (23.6 °C) is well above the annual SST_{SAT} (21.3 °C). This may be explained by the general observation that 1,15 and 1,13 diol production is weighted towards the non-upwelling season, which has above-average temperatures (as is also indicated by the poor correlation of 1,15 and 1,13 diols with 1,14 diols; Fig. 8).

Correlation is not significant between LDI and DCI ($p = 0.89$) and only just between LDI and DSI ($p = 0.045$). The DSI and DCI are solely based on 1,14 diols, and as such they are mathematically independent of the LDI. If the DSI or DCI also reflects temperature, their 1,14 diols must have been produced in a temperature regime independent of that recording the 1,15 diols.

Due to the partial absence of detected unsaturated diols, valid values of the saturation index DSI could be calculated for only half of the samples. Application of the culture-based transfer function to these samples provides unrealistic water temperatures for the CBeu surface waters (range 10.1–41.0 °C, average 33.2 °C), and this transfer function is thus not applicable to this region. The DSI lags SST_{SAT} by 76 d ($r^2 = 0.25$, $n = 58$), which is much more than observed for the LDI ($\varphi = 41$). This difference may indicate that sinking speed of the 1,14 diols (comprising the DSI) differs from that of the 1,13 and 1,15 diols (comprising the LDI). It may also be that changes in the 1,14 diol composition represent an environmental response different from the response, changing the 1,13 and 1,15 diols' composition. One explanation may be that the 1,14 diols are produced by different organisms than the 1,13 and 1,15 diols, which allows for both different sinking speeds and different environmental responses. In the marine environment, the 1,13 and 1,15 diols are predominantly derived from marine eustigmatophytes (e.g. Gelin et al., 1997; Volkman et al., 1992, 1999; Versteegh et al., 2000; Rampen et al., 2014). The 1,14C_{32} diol is a major diol in the diatom *Apedinella*
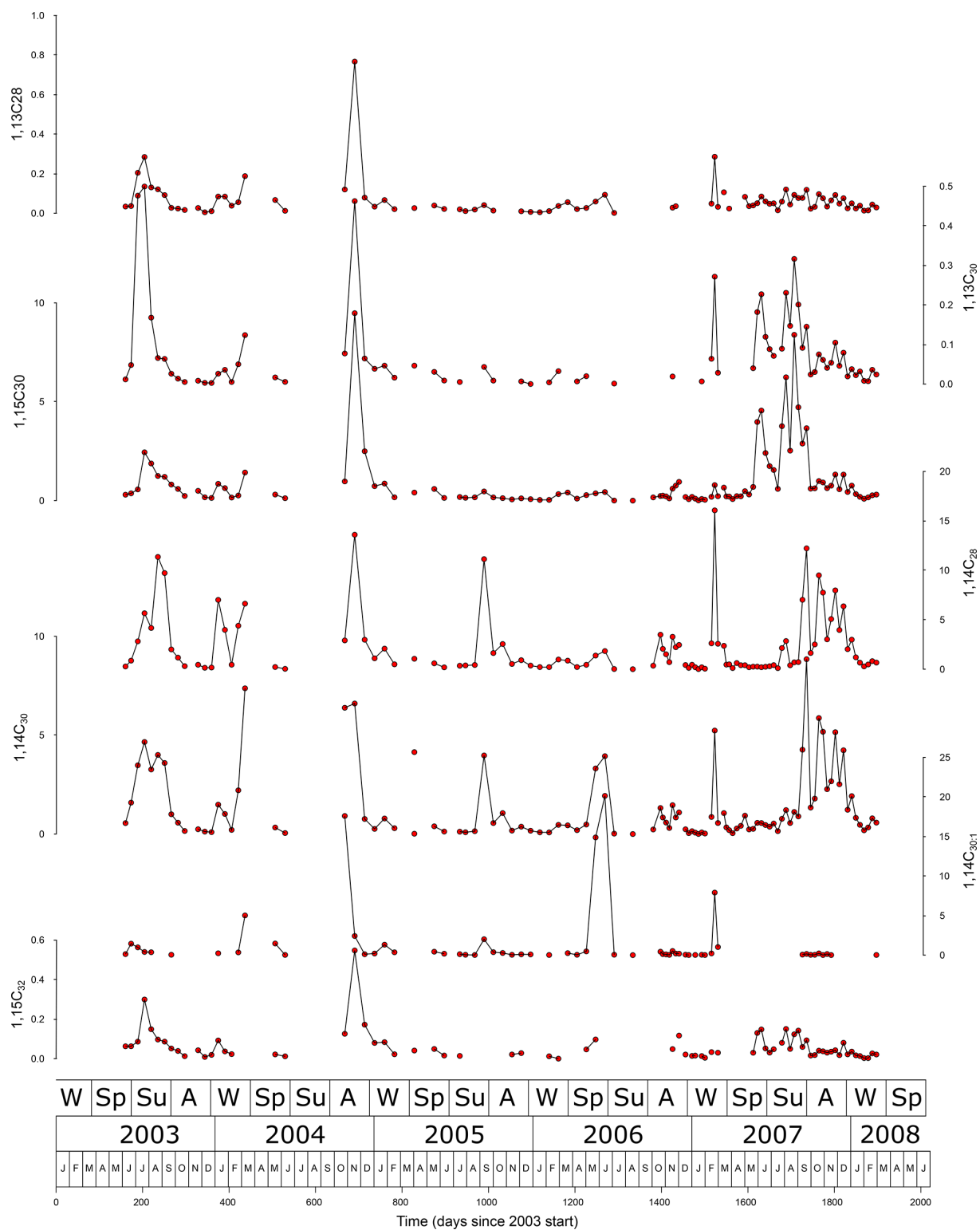
Figure 10. Fluxes for individual diols in $\mu g\,m^{-2}\,d^{-1}$.

radians (Rampen et al., 2011), but since we do not observe this diol in our cup samples, we infer that this species does not significantly contribute diols in our case. In our samples we do observe a relatively good correlation between fluxes of the diatom *Proboscia alata* and the 1,14 diols, despite possible other factors such as diatom dissolution or contribution of 1,14 diols by, as yet unknown, other sources (31 % explained variance, Fig. 9). This correlation is considerably higher than the correlation between *P. alata* fluxes and $1,13 + 1,15$ diols (4 %) or between total diatoms and 1,14 diols (17 %). This suggests that *P. alata*, as the only *Proboscia* species encountered, significantly contributes 1,14 diols, whereas its $1,13 + 1,15$ diol contribution is insignificant. Culture experiments demonstrate this ability for *P. alata* to produce 1,14 diols (Sinninghe Damsté et al., 2003). Our observations also agree well with diol data from sediment traps from the Arabian Sea where abundance of 1,14 diols covaries with upwelling and appears unrelated to the abundance of 1,15 diols (Rampen et al., 2007). Also, a recent sediment trap study from the Sea of Japan (East Sea) (Gal et al., 2021) supports the hypothesis of 1,14 diols being produced by a different plankton population than the 1,13 and 1,15 diols. In these sediment traps (March 2011–March 2012) the 1,14 diols show very similar and temporally narrowly confined flux maxima in October and November 2011, whereas the 1,13 and 1,15 diols show a very different pattern with broader flux peaks and almost permanent presence.

Assuming the upwelling-related *P. alata* being a major 1,14 diol source in our research area, it makes sense to investigate if and how the DSI relates to wind-induced upwelling and % Upw since stronger upwelling induces lower temperatures in the photic zone. During the investigated time interval, SST_{SAT} lags wind speed by about one season ($\varphi = 122$, $r^2 = 0.34$). With diatom sinking rates in this region of 100–250 m d^{-1} (Fischer and Karakaş, 2009) and 1280 m trap depth, diatoms are expected to arrive at the trap within 5–12 d after starting to sink. We observe that the abundance of upwelling species (% Upw) lags wind speed by 21 d ($r^2 = 0.26$, $p = 6.8 \times 10^{-9}$) agreeing reasonably well with the estimated sinking speed (Romero et al., 2020). We therefore expect the DSI to behave similarly to the % Upw, lagging the wind speed by 21 d and leading SST_{SAT} by 101 d. We observe the DSI lags the SST_{SAT} by 76 d and is not leading it as was assumed based on the arguments above. However, the inverse DSI (higher values, more diol unsaturation) provides a completely different picture, lagging wind speed with the same phase ($\varphi = 21$, $r^2 = 0.24$, $p = 9.7 \times 10^{-5}$) and correlating well with % Upw ($r^2 = 0.39$). It also correlates surprisingly well with SST_{SAT}, leading it by 124 d ($\varphi = -124$, $r^2 = 0.42$). We therefore propose that the inverse DSI reflects upwelling-related changes with a higher contribution of unsaturated diols upon stronger upwelling. Since upwelled waters are cool, upwelling intensity is inversely correlated with SST. Thus, the degree of 1,14 diol unsaturation reflected by the DSI could also reflect upwelling temperature. As dis-

cussed above, above CBeu, upwelling has a strong influence on the annual SST curve, with solar insolation determining SST only in summer when upwelling is weak. Furthermore, 1,14 diols seem to be primarily produced by *Proboscia*, tied to upwelling or higher nutrient levels. As such, the DSI may primarily reflect upwelling-induced temperature effects and only secondarily the temperatures resulting from direct solar radiation. Interestingly, also in the Sea of Japan sediment trap (Gal et al., 2021) the $1,14C_{28:1}$ is the only diol involved in the diol flux maximum in (cool) spring 2011, whereas all 1,14 diols are involved in the narrow diol flux peak in (warm) autumn 2011. Both these spring and autumn diol maxima occur during productivity maxima, which also show maxima of diatom export production (Kim et al., 2017). Gal et al. (2021) ascribe the spring $1,14C_{28:1}$ diol maximum to *P. alata*, whereas they relate the autumn maximum also including the $1,14C_{30}$ diols in *P. indica*, a species absent from Cap Blanc. The DSI thus seems to be heavily modulated by processes related to high productivity. Since high productivity in the ocean is temporally and spatially highly variable, a possible relation to longer-term SST_{SAT} averages may be less straightforward, and a high-resolution (sub)weekly monitoring of environment and diol production may be needed to better understand the environmental information carried by the 1,14 diol record.

The DCI leads the SST_{SAT} ($\varphi = -77$, $r^2 = 0.29$). Since the reconstructed SST cannot precede the actual SST, it is unlikely that the DCI reflects SST. Moreover, available transfer functions (see Sect. 3.4) lead to unrealistic temperatures for CBeu. The inverse of the DCI lags SST (best correlation $r^2 = 0.35$ at $\varphi = 117$), but simultaneously its average chain length decreases with temperature, which is opposite to the common physiological response of organisms to temperature (higher lipid melting point and viscosity at higher temperatures). Consequently, a causal relation through physiological adaptation of the diol-producing organisms to SST must be considered unlikely.

The DCI follows wind speed by 27–31 d ($r^2 = 0.28$, $\varphi = 27$, $p = 7.5 \times 10^{-9}$, $\varphi = 31$, $p = 6.4 \times 10^{-9}$) and upwelling species (% Upw) by 6–9 d ($r^2 = 0.42$). This suggests that like the DSI, the DCI also reflects changes in the upwelling regime. Correlations are not significant between DSI or DCI and *P. alata* fluxes. Interestingly, both these supposedly upwelling-related DSI and DCI show higher correlations to SST_{SAT} than the temperature proxy LDI. We attribute this to the (annual) cyclic nature of the system and strong influence of upwelling.

4.5 The integrated production temperature: SST_{LDI} over longer time intervals

The sediment trap intercepts the material that would continue on its way to the ocean floor 1500 m below the trap. Although the signal can be distorted on its way further to the ocean floor by (selective) degradation and transport, sed-

iment traps still provide important insight into the evaluation of the sedimentary signal. Time series from the sediment record mostly have a resolution of years to millennia, much lower than the resolution of the CBeu trap series. To get a better insight in the effect of the export dynamics as observed for CBeu on proxy values representing longer time periods, the values obtained from the individual trap cups have been weighed by the respective fluxes. For the LDI, the integrated production temperatures (IPT_{LDI}) have been calculated for a 19-cup moving window on the basis of the LDI diol fluxes and the SST_{LDI}, both with and without the SST_{LDI} outliers (Fig. 11). The LDI diol fluxes have also been combined with the SST_{SAT} at $\varphi = 41$ d (the phase relation with the best correlation). The thus obtained IPT_{SAT} represents the ideal case in which the LDI perfectly records the SST_{SAT}. The IPT_{SAT} values from January 2004–September 2005 (IPT 4 to 23) are higher than the moving-average SST_{SAT} values due to a single flux maximum in early December 2004. Considering a $\varphi = 41$ d, this production peak records high SST_{SAT} in early autumn 2004. Thus, even if the trap cups would perfectly reflect SST_{SAT}, a single flux peak may cause the IPT to differ considerably from the SST_{SAT} mean over the same period. From autumn 2005–spring 2008 the IPT_{SAT} values reflect SST_{SAT} as a result of a more constant flux magnitude.

It is obvious that even if the LDI is corrected for diol flux data (IPT_{LDI} with and without outliers), values are considerably higher than what should be reflected in the sediments (IPT_{SAT}), and they are similar to summer temperatures. In the CBeu record the high temporal resolution enables identification of outliers. With a much lower resolution (e.g. a sediment sample taken below the trap) these would be integrated in the signal. The differences between the IPT_{LDI} with and without outliers demonstrate the effect of the outliers on the IPT_{LDI}. In particular the outliers at cups centred at 204 d (10.9 °C) and 1530 d (14.9 °C) have a considerable impact since they combine low reconstructed temperatures with significant fluxes (Fig. 11). We thus demonstrate that single high fluxes and outliers in the data can have large effects on the sediment signal and this may be one reason why in higher-productivity regions such as upwelling areas correlation is less good between SST_{LDI} values in sediment surface samples and annual mean SST_{SAT}.

4.6 Diol-based productivity and nutrient concentration proxies NDI, DI_R, DI_W, and CDI

4.6.1 NDI

The NDI, DSI, and DCI correlate well ($r^2 > 0.68$). This is expected since although the NDI consists of all diols encountered, it combines the DSI and inverse DCI. The 1,14 diols in these two latter proxies obviously dominate the NDI. The NDI has been proposed to reflect NO_3^- and PO_4^{3-} concentrations in the surface waters (Gal et al., 2018, 2019, 2021). If in our setting we assume that upwelling and the relative

abundance of upwelling species (% Upw) are associated with nutrient-rich conditions at the CBeu site, a significant positive correlation between NDI and % Upw is expected. However, our results show a negative correlation (Table 4). The interpretation of the NDI as reflecting NO_3^- and PO_4^{3-} concentrations in the surface waters is further complicated by a clear annual cycle in our dataset, whereas monthly PO_4^{3-} and NO_3^- concentrations show no cyclicity. Furthermore, most concentrations of these nutrients show no correlation with the NDI ($p < 0.04$).

A closer look at the NDI reveals that the slopes of the respective transfer functions relate to each other according to the Redfield ratio N : P = 16 : 1. This may be expected since the original calibration between NDI and nutrients (Gal et al., 2018) is primarily based on sediment-derived NDI values and photic zone annual nutrient levels ($n = 216$), the latter following the Redfield ratio. SPM summer samples with associated summer nutrient concentrations are also included in this Gal et al. (2018) sediment–sea surface dataset. The NDI–PO_4^{3-} relation of these SPM samples falls within that of the sediment samples, but, for the SPM samples alone, correlation with the PO_4^{3-} concentrations is not significant ($r^2 = 0.2$, $p = 0.14$). A sediment trap study from the Sea of Japan (Gal et al., 2021) shows a different relation between the trap NDI values and monthly sea surface PO_4^{3-} concentrations ($r^2 = 0.59$, $n = 26$). In the Sea of Japan, PO_4^{3-} concentrations and NDI show a clear annual cycle. However, this is true for most environmental parameters, and it would be interesting to see what part of the observed correlation between NDI and PO_4^{3-} is causal and what part results from a common (annually cyclic) forcing factor.

4.6.2 DI_W, DI_R, and CDI

The DI_W, DI_R, and CDI have the same 1,14 diols in the numerator and only differ in the combination of 1,13 and 1,15 diols in the denominator. The CDI only adds the $1,15C_{30}$ diol to the DI_R. The DI_W has been directed as a proxy for the contribution of *Proboscia* diols relative to other diols. In our dataset, its correlation with the *Proboscia* fluxes is low but still significant ($r^2 = 0.12$, $p = 0.024$). The proxies for upwelling strength DI_R and CDI show even higher correlations with *Proboscia* (Table 4).

The DI_R has been suggested to be a proxy reflecting total export productivity. We observe high values (> 0.9) of this proxy. This would agree with the observation that this region experiences permanent upwelling. Both the DI_W and DI_R correlate negatively with wind speed (at $\varphi = 79$) and SST_{SAT} (at $\varphi = -69$). Closer observation shows that generally all diol fluxes more or less covary except in 2007 when pulses in 1,13 and 1,15 diols precede those of the 1,14 diols (Fig. 8) and the DI_R sinks below 0.8. Comparison to the total mass flux (correlation insignificant) and to the % Upw reveals that this change in diol composition is not accompanied by a consistent change in export flux so that an expla-
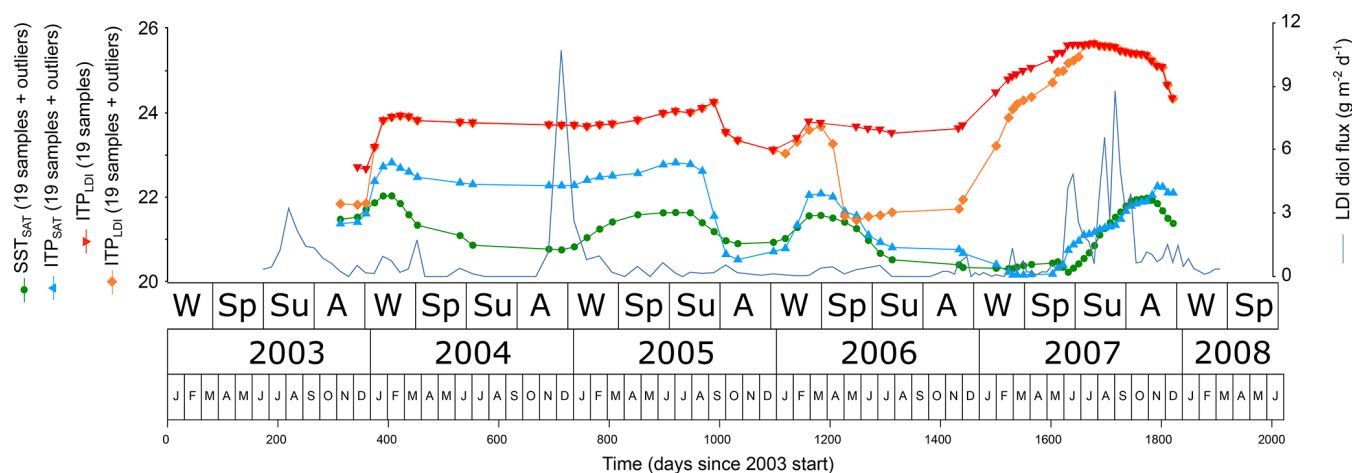
Figure 11. The 19-sample moving-average SST_{SAT} (green spheres) and 19-sample moving-integrated production temperatures for SST_{SAT} (IPT_{SAT}, blue upward triangles) and for SST_{LDI} (IPT_{LDI}, orange diamonds), both based on the LDI diol fluxes and the respective SST records. Samples with LDI outliers (values $<17\,°C$) are included except for the upper graph of IPT_{LDI} (red downward pointing triangles). For reference, the LDI diol flux is included as well.

nation for the relative increase in 1,15 diols seems to require a more subtle knowledge of the relation between diol abundance and environment on the CBeu trap data alone.

Other trap studies reporting diol fluxes from tropical Atlantic are upper traps from 1150 m depth in the eastern Atlantic near the Guinea Dome and influenced by seasonal upwelling (M1U), from 1235 m depth in the oligotrophic Central Atlantic (M2U) and from 1130 m depth in the western Atlantic and under seasonal influence from the Amazon outflow (M4U) (de Bar et al., 2019). It appears that for the $1,13+1,15$ diols our average of $3.9\,\mu g\,m^{-2}\,d^{-1}$ for CBeu5 is only 1.5 times the average for the nearest trap M1U ($2.6\,\mu g\,m^{-2}\,d^{-1}$) and about 3 times the flux of the oligotrophic central Atlantic M2U ($1.2\,\mu g\,m^{-2}\,d^{-1}$) but only half that of the westernmost M4U ($7\,\mu g\,m^{-2}\,d^{-1}$). For the 1,14 diols the average of $1.7\,\mu g\,m^{-2}\,d^{-1}$ for CBeu5 is at least 3 times higher than for the other traps (0.5 for M1U, 0.01 for M2U, and 0.3 for M4U). Since CBeu5 is the only site under permanent upwelling influence, we infer that the 1,14 diols are particularly abundant in the (coastal) upwelling whereas the 1,13 and 1,15 diols also increase with increasing productivity but seem to be less bound to upwelling and possibly better reflect the more oligotrophic open ocean (agreeing with Versteegh et al., 2000; Rampen et al., 2008). Seen in this light, it may be expected that at CBeu the SST_{LDI} values reflect summer SST_{SAT} since the oligotrophic open ocean conditions are largely constrained to the short (July–October) period with high temperatures.

4.7 $U_{37}^{K'}$ and SST_{UK}

The 35 d phase lag of SST_{UK} relative to SST_{SAT} suggests that it takes about 1 month between fixation of the alkenone composition in the cell and the collection of the alkenones

in the cup of the sediment trap, which implies an average sinking rate of $38\,m\,d^{-1}$.

The complex cubic transformation of $U_{37}^{K'}$ values to SST_{UK} for SPM derived from a global dataset (Conte et al., 2006) has a lower correlation than $U_{37}^{K'}$ itself. This implies that in this case a linear transformation would have performed equally well. This we may expect since our data cover only a fraction (18–$27\,°C$) of the global temperature range, and for this fraction the cubic transformation behaves almost linearly. Since the explained variance is much lower ($60\,\%$) than for the global calibration ($97\,\%$), we infer that other factors than surface water temperature influence the alkenone composition. If the reconstructed SST_{UK} would perfectly project to the SST_{SAT}, the slope of the regression would be 1 and the intercept 0. However, the slope of the SST_{UK} regression to binned SST_{SAT} is 0.72 and the intercept 5.6, which implies that the global SPM calibration overestimates local SST_{SAT} below $20\,°C$ and underestimates local values above this temperature. If we assume that the global calibration is correct and the alkenones reflect the water temperature the organisms were subject to, the conclusion would be that above $20\,°C$ the organisms live in water that is slightly cooler than that at the sea surface (SST_{SAT}) and slightly warmer below this temperature. This could be explained by a higher influence of solar irradiation at the sea surface than at the subsurface. This is only feasible if the alkenone-producing organisms live partly or entirely below the surface mixed layer. Surface currents are from the NE where (upwelling) SST is lower. Therefore, admixture of alkenones produced upstream could also be an explanation. Alternatively, we may adjust the SPM calibration of Conte et al. (2006) such that we obtain a local calibration where the slope and intercept agree with the binned SST_{SAT} data ($\varphi = 35$), providing (see also

Fig. S3)

$$\mathrm{SST_{UK}}\ (^{\circ}\mathrm{C}) = 0.64733 + 54.293\mathrm{U}_{37}^{\mathrm{K}'}$$
$$- 52.894\left(\mathrm{U}_{37}^{\mathrm{K}'}\right)^2 + 23.382\left(\mathrm{U}_{37}^{\mathrm{K}'}\right)^3, \qquad (20)$$

with $\varphi = 33$ and $r^2 = 0.54$. Just like the global calibration of Conte et al. (2006), this regional calibration shows a higher correlation to $\mathrm{SST_{SAT}}$ than any of the diol proxies discussed above.

5   Conclusions

The variation in diol, fluxes, and relative abundances as observed in sediment trap cups off Mauritania from 2003 to 2008 have been compared with environmental conditions and alkenone and plankton composition for the same region and time period. From this comparison, the following is concluded.

1. Peak total mass fluxes of material to the sediment trap do not show a statistically significant annual cycle but may occur throughout the year. Nevertheless, total mass flux maxima are most abundant during spring. We explain this rather unpredictable occurrence of these flux maxima by attributing them to the passage of upwelling filaments over the sediment trap, which occurs most often during spring, but is not limited to this.

2. Off Cap Blanc, upwelling variability is the major environmental variable. It shows a strong annual cycle in response to the strength of the trade winds. Sea surface temperature also shows a strong annual cycle, remaining low in winter and during vernal upwelling and following insolation when upwelling is reduced during summer. It lags upwelling by 130 d. As a result of the predominant annual cycle in both temperature and upwelling, correlations between parameters and/or proxy records should be interpreted with care, and phase relations should be considered to identify the most likely forcing mechanism.

3. The alkenone-based $\mathrm{U}_{37}^{\mathrm{K}'}$ lags SST by 35 d and excellently reconstructs SST with respect to both amplitude and absolute values.

4. The diol-derived LDI lags SST by 41 d. It correlates only weakly with SST. On average the $\mathrm{SST_{LDI}}$ reflects the high $\mathrm{SST_{SAT}}$ prevalent during the more oligotrophic summer period. The LDI shows several outliers to very low reconstructed temperatures, which we attribute to an additional source of 1,13 diols and which have a considerable influence on the low-resolution $\mathrm{SST_{LDI}}$ signal as may be encountered in the underlying sediment.

5. The diol-derived nutrient index NDI, the DCI, and the percentage of upwelling species show a higher correlation to SST than the LDI. However, they lead the SST by several months, and their variability is most likely a response to upwelling-associated processes such as a reduction in temperature, increased nutrient content, and modified species composition. A rather intriguing result is the anticorrelation between the diol-derived nutrient proxy NDI and upwelling intensity.

Author contributions. GJMV interpreted the data and wrote most of the paper. KAFZ discussed and edited the paper prior to submission. JH processed the lipid analyses of CBeu5 and contributed to the Material and methods section. OER contributed the diatom data and together with GM critically reviewed earlier versions of the paper. GF coordinated the sediment trap project.

References

Brassell, S. C., Eglinton, G., Marlowe, I. T., Pflaumann, U., and Sarnthein, M.: Molecular stratigraphy: a new tool for climatic assessment, Nature, 320, 129–133, https://doi.org/10.1038/320129a0, 1986.

Chavez, F. P. and Messié, M.: A comparison of eastern boundary upwelling ecosystems, Prog. Oceanogr., 83, 80–96, https://doi.org/10.1016/j.pocean.2009.07.032, 2009.

Conte, M. H., Sicre, M. A., Rühlemann, C., Weber, J. C., Schulte, S., Schulz-Bull, D., and Blanz, T.: Global temperature calibration of the alkenone unsaturation index ($U_{37}^{K'}$) in surface waters and comparison with surface sediments, Geochem. Geophy. Geosy., 7, Q02005, https://doi.org/10.1029/2005GC001054, 2006.

Cropper, T. E., Hanna, E., and Bigg, G. R.: Spatial and temporal seasonal trends in coastal upwelling off Northwest Africa, 1981–2012, Deep-Sea Res. Pt. I, 86, 94–111, https://doi.org/10.1016/j.dsr.2014.01.007, 2014.

de Bar, M. W., Ullgren, J. E., Thunnell, R. C., Wakeham, S. G., Brummer, G.-J. A., Stuut, J.-B. W., Sinninghe Damsté, J. S., and Schouten, S.: Long-chain diols in settling particles in tropical oceans: insights into sources, seasonality and proxies, Biogeosciences, 16, 1705–1727, https://doi.org/10.5194/bg-16-1705-2019, 2019.

de Bar, M. W., Weiss, G., Yildiz, C., Rampen, S. W., Lattaud, J., Bale, N. J., Mienis, F., Brummer, G.-J. A., Schulz, H., Ruch, D., Kim, J.-H., Donner, B., Knies, J., Lückge, A., Stuut, J.-B. W., Sinninghe Damsté, J. S., and Schouten, S.: Global temperature calibration of the Long chain Diol Index in marine surface sediments, Org. Geochem., 142, 103983, https://doi.org/10.1016/j.orggeochem.2020.103983, 2020.

de Leeuw, J. W., Rijpstra, W. I. C., and Schenck, P. A.: The occurrence and identification of C_{30}, C_{31} and C_{32} alkan-1,15-diols and alkan-15-on-1-ols in Unit I and Unit II Black Sea sediments, Geochim. Cosmochim. Ac., 45, 2281–2285, https://doi.org/10.1016/0016-7037(81)90077-6, 1981.

Elling, F. J., Könneke, M., Mußmann, M., Greve, A., and Hinrichs, K.-U.: Influence of temperature, pH, and salinity on membrane lipid composition and TEX_{86} of marine planktonic thaumarchaeal isolates, Geochim. Cosmochim. Ac., 171, 238–255, https://doi.org/10.1016/j.gca.2015.09.004, 2015.

Fischer, G. and Karakaş, G.: Sinking rates and ballast composition of particles in the Atlantic Ocean: implications for the organic carbon fluxes to the deep ocean, Biogeosciences, 6, 85–102, https://doi.org/10.5194/bg-6-85-2009, 2009.

Gabric, A. J., Garcia, L., Camp, L. V., Nykjaer, L., Eifler, W., and Schrimpf, W.: Offshore export of shelf production in the Cape Blanc (Mauritania) giant filament as derived from coastal zone color scanner imagery, J. Geophys. Res., 98, 4697–4712, https://doi.org/10.1029/92JC01714, 1993.

Gal, J.-K., Kim, J.-H., and Shin, K.-H.: Distribution of long chain alkyl diols along a south-north transect of the northwestern Pacific region: Insights into a paleo sea surface nutrient proxy, Org. Geochem., 119, 80–90, https://doi.org/10.1016/j.orggeochem.2018.01.010, 2018.

Gal, J.-K., Kim, J.-H., Kim, S., Lee, S. H., Yoo, K.-C., and Shin, K.-H.: Application of the newly developed nutrient diol index (NDI) as a sea surface nutrient proxy in the East Sea for the last 240 years, Quat. Intern., 503, 146–152, https://doi.org/10.1016/j.quaint.2018.11.003, 2019.

Gal, J.-K., Kim, J.-H., Kim, S., Hwang, J., and Shin, K.-H.: Assessment of the nutrient diol index (NDI) as a sea surface nutrient proxy using sinking particles in the East Sea, Mar. Chem., 231, 103937, https://doi.org/10.1016/j.marchem.2021.103937, 2021.

Garcia, H. E., Weathers, K., Paver, C. R., Smolyar, I., Boyer, T. P., Locarnini, M. M., Zweng, M. M., Mishonov, A. V., Baranova, O. K., Seidov, D., and Reagan, J. R.: World Ocean Atlas 2018, Vol. 4: Dissolved Inorganic Nutrients (phosphate, nitrate and nitrate + nitrite, silicate), Mishonov, A., Technical Editor, Silver Spring MD, NOAA Atlas NESDIS 84 [data set], p. 35, https://www.ncei.noaa.gov/access/world-ocean-atlas-2018/bin/woa18.pl?parameter=p (last access: 10 March 2022), https://www.ncei.noaa.gov/access/world-ocean-atlas-2018/bin/woa18.pl?parameter=n (last access: 10 March 2022), 2019.

Gelin, F., Boogers, I., Noordeloos, A. A. M., Sinninghe Damsté, J. S., Riegman, R., and de Leeuw, J. W.: Resistant biomacromolecules in marine microalgae of the classes Eustigmatophyceae and Chlorophyceae: Geochemical applications, Org. Geochem., 26, 659–675, https://doi.org/10.1016/S0146-6380(97)00035-1, 1997.

Grange, S. K.: Technical note: Averaging wind speeds and directions, https://doi.org/10.13140/RG.2.1.3349.2006, 2014.

Hammer, Ø., Harper, D. A. T., and Ryan, P. D.: PAST: Paleontological statistics software package for education and data analysis, Palaeontol. Electron., 4, 1–9, 2001.

Huang, B., Liu, C., Banzon, V. F., Freeman, E., Graham, G., Hankins, B., Smith, T., and Zhang, H.-M.: NOAA 0.25-degree daily optimum interpolation sea surface temperature (OISST), Version 2.1, Dataset ncdcOisst21Agg_LonPM180, NOAA National Centers for Environmental Information [data set], https://doi.org/10.25921/RE9P-PT57, 2020.

Kim, M., Hwang, J., Rho, T., Lee, T., Kang, D.-J., Chang, K.-I., Noh, S., Joo, H., Kwak, J. H., Kang, C.-K., and Kim, K.-R.: Biogeochemical properties of sinking particles in the southwestern part of the East Sea (Japan Sea), J. Marine Syst., 167, 33–42, https://doi.org/10.1016/j.jmarsys.2016.11.001, 2017.

Kremling, K., Lentz, U., Zeitzschel, B., Schulz-Bull, D. E., and Duinker, J. C.: New type of time-series sediment trap for the reliable collection of inorganic and organic trace chemical substances, Rev. Sci. Instrum., 67, 4360, https://doi.org/10.1063/1.1147582, 1998.

Lathuilière, C., Echevin, V., and Lévy, M.: Seasonal and intraseasonal surface chlorophyll-a variability along the northwest African coast, J. Geophys. Res., 113, C05007, https://doi.org/10.1029/2007JC004433, 2008.

Lattaud, J., Dorhout, D., Schulz, H., Castañeda, I. S., Schefuß, E., Sinninghe Damsté, J. S., and Schouten, S.: The C_{32} alkane-1,15-diol as a proxy of late Quaternary riverine input in coastal margins, Clim. Past, 13, 1049–1061, https://doi.org/10.5194/cp-13-1049-2017, 2017a.

Lattaud, J., Kim, J.-H., De Jonge, C., Zell, C., Sinninghe-Damsté, J. S., and Schouten, S.: The C_{32} alkane-1,15-diol as a tracer for riverine input in coastal seas, Geochim. Cosmochim. Ac., 202, 146–158, https://doi.org/10.1016/j.gca.2016.12.030, 2017b.

Locarnini, M. M., Mishonov, A. V., Baranova, O. K., Boyer, T. P., Zweng, M. M., Garcia, H. E., Reagan, J. R., Seidov, D., Weathers, K., Paver, C. R., and Smolyar, I.: World ocean atlas 2018, Vol 1: Temperature, Mishonov, A., Technical Edi-

tor, Silver Spring MD, NOAA Atlas NESDIS 81 [data set], p. 52., https://www.ncei.noaa.gov/access/world-ocean-atlas-2018/bin/woa18.pl?parameter=t (last access: 10 March 2022) 2018.

Lovecchio, E., Gruber, N., Münnich, M., and Lachkar, Z.: On the long-range offshore transport of organic carbon from the Canary Upwelling System to the open North Atlantic, Biogeosciences, 14, 3337–3369, https://doi.org/10.5194/bg-14-3337-2017, 2017.

Lovecchio, E., Gruber, N., and Münnich, M.: Mesoscale contribution to the long-range offshore transport of organic carbon from the Canary Upwelling System to the open North Atlantic, Biogeosciences, 15, 5061–5091, https://doi.org/10.5194/bg-15-5061-2018, 2018.

Mollenhauer, G., Basse, A., Kim, J.-H., Sinninghe Damsté, J. S., and Fischer, G.: A four-year record of $U_{37}^{K'}$- and TEX_{86}-derived sea surface temperature estimates from sinking particles in the filamentous upwelling region off Cape Blanc, Mauritania, Deep-Sea Res. Pt. I, 97, 67–79, https://doi.org/10.1016/j.dsr.2014.11.015, 2015.

Müller, P. J., Kirst, G., Ruhland, G., Von Storch, I., and Rosell-Melé, A.: Calibration of the alkenone paleotemperature index based on coretops from the eastern South Atlantic and global ocean (60° N–60° S), Geochim. Cosmochim. Ac., 62, 1757–1772, https://doi.org/10.1016/S0016-7037(98)00097-0, 1998.

Prahl, F. G. and Wakeham, S. G.: Calibration of unsaturation patterns in long-chain ketone compositions for palaeotemperature assessment, Nature, 330, 367–369, https://doi.org/10.1038/330367a0, 1987.

Rampen, S. W., Schouten, S., Wakeham, S. G., and Sinninghe Damsté, J. S.: Seasonal and spatial variation in the sources and fluxes of long chain diols and mid-chain hydroxy methyl alkanoates in the Arabian Sea, Org. Geochem., 38, 165–179, https://doi.org/10.1016/j.orggeochem.2006.10.008, 2007.

Rampen, S. W., Schouten, S., Koning, E., Brummer, G.-J. A., and Sinninghe Damsté, J. S.: A 90 kyr upwelling record from the northwestern Indian Ocean using a novel long-chain diol index, Earth Planet. Sc. Lett., 276, 207–213, https://doi.org/10.1016/j.epsl.2008.09.022, 2008.

Rampen, S. W., Schouten, S., Schefuß, E., and Sinninghe Damsté, J. S.: Impact of temperature on long chain diol and mid-chain hydroxy methyl alkanoate composition in *Proboscia* diatoms: Results from culture and field studies, Org. Geochem., 40, 1124–1131, https://doi.org/10.1016/j.orggeochem.2009.08.005, 2009.

Rampen, S. W., Schouten, S., and Sinninghe Damsté, J. S.: Occurrence of long chain 1,14-diols in Apedinella radians, Org. Geochem., 42, 572–574, https://doi.org/10.1016/j.orggeochem.2011.03.009, 2011.

Rampen, S. W., Willmott, V., Kim, J.-H., Uliana, E., Mollenhauer, G., Schefuß, E., Sinninghe Damsté, J. S., and Schouten, S.: Long chain 1,13- and 1,15-diols as a potential proxy for palaeotemperature reconstruction, Geochim. Cosmochim. Ac., 84, 204–216, https://doi.org/10.1016/j.gca.2012.01.024, 2012.

Rampen, S. W., Willmott, V., Kim, J.-H., Rodrigo-Gámiz, M., Uliana, R. E., Mollenhauer, G., Schefuß, E., Sinninghe Damsté, J. S., and Schouten, S.: Evaluation of long chain 1,14-alkyl diols in marine sediments as indicators for upwelling and temperature., Org. Geochem., 76, 39–47, https://doi.org/10.1016/j.orggeochem.2014.07.012, 2014.

Redfield, A. C., Ketchum, B. H., and Richards, F. A.: The influence of organisms on the composition of sea-water, in: The Sea, edited by: Hill, M. N., Interscience, New York, 26–77, 554 pp., ISBN 978-0-674-01728-3, 1963.

Romero, O. E., Baumann, K.-H., Zonneveld, K. A. F., Donner, B., Hefter, J., Hamady, B., Pospelova, V., and Fischer, G.: Flux variability of phyto- and zooplankton communities in the Mauritanian coastal upwelling between 2003 and 2008, Biogeosciences, 17, 187–214, https://doi.org/10.5194/bg-17-187-2020, 2020.

Saha, K., Zhao, X., Zhang, H.-M., Casey, K. S., Zhang, D., Baker-Yeboah, S., Kilpatrick, K. A., Evans, R. H., Ryan, T., and Relph, J. M.: AVHRR Pathfinder version 5.3 level3 collated (L3C) global 4 km sea surface temperature for 1981-Present, Dataset nceiPH53sstn1day_Lon360, NOAA National Centers for Environmental Information [data set], https://doi.org/10.7289/v52j68xx, 2018.

Sinninghe Damsté, J. S., Rampen, S., Rijpstra, W. I. C., Abbas, B., Muyzer, G., and Schouten, S.: A diatomaceous origin for long-chain diols and mid-chain hydroxy methyl alkanoates widely occurring in Quaternary marine sediments: Indicators for high-nutrient conditions, Geochim. Cosmochim. Ac., 67, 1339–1348, https://doi.org/10.1016/S0016-7037(02)01225-5, 2003.

Sollich, M., Yoshinaga, M. Y., Häusler, S., Price, R. E., Hinrichs, K.-U., and Bühring, S. I.: Heat stress dictates microbial lipid composition along a thermal gradient in marine sediments, Front. Microbiol., 8, 1550, https://doi.org/10.3389/fmicb.2017.01550, 2017.

Suutari, M. and Laakso, S.: Microbial fatty acids and thermal adaptation, Crit. Rev. Microbiol., 20, 285–328, https://doi.org/10.3109/10408419409113560, 1994.

Versteegh, G. J. M., Bosch, H. J., and de Leeuw, J. W.: Potential palaeoenvironmental information of C_{24} to C_{30} mid-chain diols, keto-ols and mid-chain hydroxy fatty acids; a critical review, Org. Geochem., 27, 1–13, https://doi.org/10.1016/S0146-6380(97)00063-6, 1997.

Versteegh, G. J. M., Jansen, J. H. F., de Leeuw, J. W., and Schneider, R. R.: Mid-chain diols and keto-ols in SE Atlantic sediments. A new tool for tracing past sea surface water masses?, Geochim. Cosmochim. Ac., 64, 1879–1892, https://doi.org/10.1016/S0016-7037(99)00398-1, 2000.

Versteegh, G. J. M., Zonneveld, K. A. F., Hefter, J., Romero, O. E., Fischer, G., and Mollenhauer, G.: long-chain 1, mid-chain alkane-diol and accompanying environmental data for CBeu sediment trap (off Mauritania) samples from 2003 to 2008, PANGAEA [data set], https://doi.pangaea.de/10.1594/PANGAEA.940305, 2022.

Volkman, J. K., Barrett, S. M., Dunstan, G. A., and Jeffrey, S. W.: C_{30}–C_{32} alkyl diols and unsaturated alcohols in microalgae of the class Eustigmatophyceae, Org. Geochem., 18, 131–138, https://doi.org/10.1016/0146-6380(92)90150-V, 1992.

Volkman, J. K., Barrett, S. M., and Blackburn, S. I.: Eustigmatophyte microalgae are potential sources of C_{29} sterols, C_{22}–C_{28} *n*-alcohols and C_{28}–C_{32} *n*-alkyl diols in freshwater environments, Org. Geochem., 30, 307–318, https://doi.org/10.1016/S0146-6380(99)00009-1, 1999.

Willmott, V., Rampen, S. W., Domack, E., Canals, M., Sinninghe Damsté, J. S., and Schouten, S.: Holocene changes in *Proboscia* diatom productivity in shelf waters of the north-western Antarctic Peninsula, Antarct. Sci., 22, 3–10, https://doi.org/10.1017/S095410200999037X, 2010.

Zweng, M. M., Reagan, J. R., Seidov, D., Boyer, T. P., Locarnini, M. M., Garcia, H. E., Mishonov, A. V., and Baranova, O. K.: World ocean atlas 2018, Vol. 2: Salinity, edited by: , Weathers, K. W., Paver, C. R., and Smolyar, I. V., Mishonov, A., Technical Editor, Silver Spring MD, NOAA Atlas NESDIS 82 [data set], p. 50, https://www.ncei.noaa.gov/access/world-ocean-atlas-2018/bin/woa18.pl?parameter=s (last access: 10 March 2022), 2019.